applied sciences

MDPI

Article

Comparison of Acceleration Amplification for Seismic Behavior Characteristics Analysis of Electrical Cabinet Model: Experimental and Numerical Study

Da-Woon Yun [1], Bub-Gyu Jeon [1,*], Sung-Wan Kim [1,*], Daegi Hahm [2] and Hong-Pyo Lee [3]

[1] Seismic Research and Test Center, Pusan National University, 49, Busandaehak-ro, Yangsan 50612, Republic of Korea; ardw818@pusan.ac.kr
[2] Structural and Seismic Safety Research Division, Korea Atomic Energy Research Institute, 111, Daedeok-daero 989beon-gil, Daejeon 34057, Republic of Korea
[3] Central Research Institute, Korea Hydro & Nuclear Power Co., Ltd., 70, Yuseong-daero 1312beon-gil, Daejeon 34101, Republic of Korea; hongpyo.lee@khnp.co.kr
* Correspondence: bkjeon79@pusan.ac.kr (B.-G.J.); swkim09@pusan.ac.kr (S.-W.K.)

Abstract

Given the critical role of electrical cabinets in the post-earthquake recovery and emergency response of nuclear power plants (NPPs), a comprehensive assessment of their seismic performance is essential to ensure operational safety. This study analyzed seismic behavior by fabricating an electrical cabinet model based on the dynamic characteristics and field surveys of equipment installed in a Korean-type NPP. A shaking table test with simultaneous tri-axial excitation was conducted, incrementally increasing the seismic motion until damage was observed. A numerical model was then developed based on the experimental results, followed by a seismic response analysis and comparison of results. The findings verified that assuming fixed anchorage conditions in the numerical model may significantly overestimate seismic performance, as it fails to account for the nonlinear behavior of the anchorage system, as well as the superposition between global and local modes caused by cabinet rocking and impact under strong seismic loading. Furthermore, damage and impact at the anchorage amplified acceleration responses, significantly affecting the high-frequency range and the vertical behavior, leading to substantial amplification of the in-cabinet response spectrum.

Keywords: electrical cabinet; shaking table test; numerical analysis; acceleration amplification; seismic behavior

check for updates

Academic Editors: Ivan Kraus and Davide Lavorato

Received: 9 June 2025
Revised: 25 June 2025
Accepted: 26 June 2025
Published: 27 June 2025

Citation: Yun, D.-W.; Jeon, B.-G.; Kim, S.-W.; Hahm, D.; Lee, H.-P. Comparison of Acceleration Amplification for Seismic Behavior Characteristics Analysis of Electrical Cabinet Model: Experimental and Numerical Study. *Appl. Sci.* **2025**, *15*, 7274. https://doi.org/10.3390/app15137274

Copyright: © 2025 by the authors. Licensee MDPI, Basel, Switzerland. This article is an open access article distributed under the terms and conditions of the Creative Commons Attribution (CC BY) license (https://creativecommons.org/licenses/by/4.0/).

1. Introduction

Beyond the immediate physical damage caused by earthquakes, disruptions or failures of power systems within critical infrastructure can result in considerable economic loss and increased casualties. Since power facilities are essential for post-earthquake emergency response and recovery, their protection is paramount [1,2]. Electrical cabinets, in particular, are vital components of nuclear power plants (NPPs), widely deployed to support essential operational functions [3]. Accordingly, the U.S. Nuclear Regulatory Commission (USNRC) emphasizes the importance of evaluating the dynamic behavior of electrical cabinets to ensure NPP safety [4,5]. Similarly, the International Atomic Energy Agency (IAEA) recommends experimental evaluation of such complex components [6]. Numerous studies have employed shaking table tests to evaluate the seismic performance of electrical cabinets [7–11].

Experimental studies have been conducted to evaluate the seismic performance of electrical cabinets installed in critical facilities, such as telecommunication systems, that are designed to maintain essential functions [12,13]. Further experimental research has aimed to enhance seismic performance through cabinet base reinforcement, using tuned mass dampers, and analysis of cabinet grouping effects [14–16]. However, comprehensive experimental evaluations covering a broad range of seismic parameters, such as various seismic waves, require considerable financial investment. Furthermore, testing in-service equipment is often subject to operational limitations, including the need for system shutdown or component disassembly. Therefore, numerical studies based on shaking table test results are generally conducted to account for multiple seismic parameters cost-effectively and practically [17–22].

The base frame of an electrical cabinet, having lower rigidity than its main structural members, is typically mounted to a concrete foundation using anchor bolts. These cabinets may experience torsional effects under seismic loading [23]. In addition, as shown in Figure 1, rocking behavior can occur due to uplifting caused by cup-like deformation of the base frame around the anchor bolts. The dominant seismic behavior includes global modes in the two horizontal directions, which manifest as rocking coupled with bending [24,25]. These dynamics have been explored in previous studies [22,25–27]. As shown in Figure 2, cabinets without anchorage typically fail by overturning, whereas those firmly anchored tend to fail through anchor bolt rupture or concrete cracking, often accompanied by rocking [1,28]. Rattling, banging, and internal impacts are also induced by the uplifting and rocking of the cabinet. These impacts can significantly amplify the in-cabinet response spectrum (ICRS), particularly in the high-frequency ranges above 20 Hz [17,29]. Given the high sensitivity of cabinet systems to high-frequency excitation, such amplified responses may adversely affect the structural integrity and functional reliability of internal devices, potentially introducing new failure modes and functional issues [30]. These amplifications vary spatially within the cabinet, peaking where global and local modes interact or where local modes dominate due to internal impacts [31]. Therefore, accurately reflecting the realistic seismic behavior in numerical models is essential when evaluating the seismic performance of electrical cabinets using numerical methods.

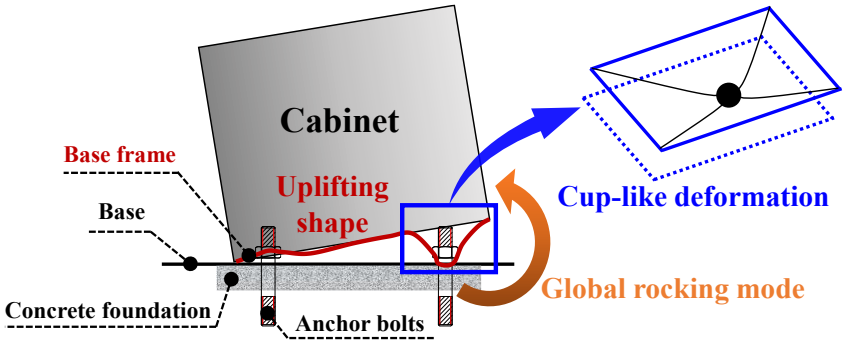


Figure 1. Description of base frame deformation and rocking behavior of the cabinet.

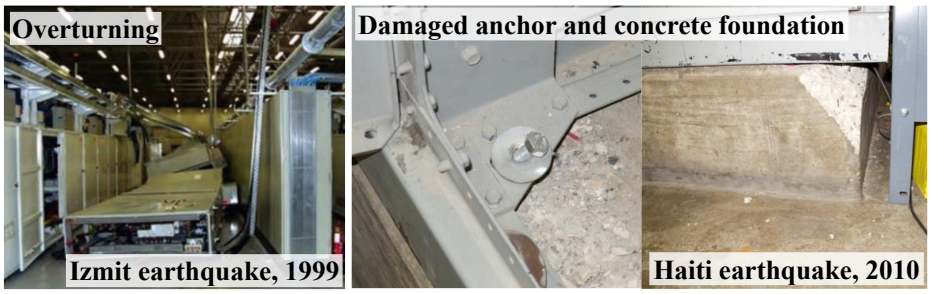


Figure 2. Earthquake damage to electrical cabinets [1,28].

Most numerical models simplify anchorage boundary conditions by assuming rigid fixation to the foundation [20,22]. However, the flexibility of the base frame significantly varies depending on weld quality, anchor bolt characteristics, specific mounting arrangements, and structural details, making it difficult to directly incorporate these factors into numerical models [24,32–34]. In particular, constraining the vertical degree of freedom at the anchorage can result in deformation occurring below the foundation level due to cup-like deformation at the base frame (Figure 1). However, such downward displacement is physically restricted in actual behavior. The anchorage system exhibits nonlinear behavior, and inaccurate modeling of boundary conditions at the anchorage can result in erroneous predictions of seismic response [25]. Recent studies have found that simplified constraints on anchorage degrees of freedom may lead to overestimation of cabinet seismic performance, recommending the incorporation of the hysteretic behavior of anchor bolts to better represent cabinet–foundation interaction effects [27,35]. Furthermore, studies reveal that modeling torque loosening induced by cabinet dynamics is limited in its effectiveness [36]. While numerical methods are more cost-effective than experimental approaches, their predictive accuracy is limited by the complexity of accurately modeling anchorage behavior. In addition, numerical studies based on shaking table test results often evaluate seismic behavior by validating only the natural frequencies and modal properties of numerical models, or by considering only unidirectional or horizontal seismic motions [12,20]. At relatively low seismic load levels, experimental and numerical results have shown good agreement, resulting in potentially conservative assessments of numerical methods in some cases [37]. Under such low-seismic load conditions, the previously discussed nonlinear anchorage behavior, cabinet rocking, and impact phenomena may not manifest. However, as the seismic load increases, critical responses such as the superposition of global and local modes, yielding of anchor bolts, and deformation of the base frame may go unaccounted for in simplified models, thus requiring careful consideration [25]. Therefore, it is necessary to verify and compare the actual seismic behavior under relatively strong tri-axial seismic loads, including vertical components, which can induce nonlinear anchorage behavior, cabinet rocking, and impact phenomena, with the behavior predicted by numerical models.

This study aimed to investigate the seismic behavior of electrical cabinets through a combined experimental and numerical approach. A specimen was designed by fabricating an electrical cabinet model that reflects the dynamic characteristics of electrical equipment installed in Korean-type NPPs and the geometry of a motor control center (MCC), along with a foundation anchorage configured based on field survey. An experimental study was conducted using a simplified model of the newly designed electrical cabinet. Tri-axial shaking table tests were conducted under progressively increasing seismic loads until damage occurred. The anchorage boundary condition was modeled as a fixed support, as is commonly assumed in numerical approaches, to construct the numerical model. The numerical model's validity was verified using the shaking table test results, and a seismic response analysis was conducted with the same input seismic motions. The amplification of the acceleration response was analyzed based on the experimental and numerical results to differentiate seismic behavior characteristics between the two methods.

2. Experimental Test Overview

2.1. Design and Fabrication of Specimen

As part of the specimen configuration, the electrical cabinet model was anchored to a concrete foundation with a design strength of 27 MPa and a thickness of 150 mm, considering the structural design of NPP facilities and testing requirements. Field surveys confirmed that typical electrical cabinets are anchored using 4 to 8 anchor bolts, generally ranging from M10 to M12 in size. To represent a conservative and more vulnerable anchor-

age condition, four M10 anchor bolts were employed. The anchor bolts were fabricated in accordance with ACI standards and ASTM A36 specifications and installed using a cast-in-place method integrated into the concrete foundation [38,39]. The embedment depth was set at 80 mm, considering the concrete foundation thickness.

In grouped installations of multiple electrical cabinets, collective systems exhibit internal damping and energy dissipation. Accordingly, the ICRS and dynamic behavior can be reasonably represented by evaluating a single cabinet [40–42]. To simulate a vulnerable condition, the specimen was configured as an independent, single-bay installation, deliberately excluding grouping effects. The dynamic characteristics of the electrical cabinet model were designed with reference to previous shaking table tests conducted to assess the seismic performance of safety-related electrical equipment in Korean-type NPPs [43,44]. As synthesized in Table 1, this equipment exhibits an average resonant frequency of approximately 18 Hz. Moreover, field tests using an impact hammer on actual NPP equipment indicated an average frequency range of 15–17 Hz. The specimen adopted an MCC configuration, and the target natural frequency range was set between 15 and 18 Hz, based on both experimental and field measurements. Stiffeners were installed at the anchorage to establish directional stiffness along weak and strong axes in the horizontal plane, ensuring that the first and second mode frequencies fell within the designated range. A preliminary numerical model was created using the numerical analysis software ABAQUS version 6.14 to guide the design and fabrication process. Rectangular hollow sections conforming to KS D 3568 were selected, with adjusted dimensions and mass properties to achieve the target dynamic characteristics [45]. For the eigenvalue analysis, the cabinet base was modeled as a fully fixed support. The final specimen geometry and configuration, as illustrated in Figure 3, were determined based on stiffness and mass distribution.

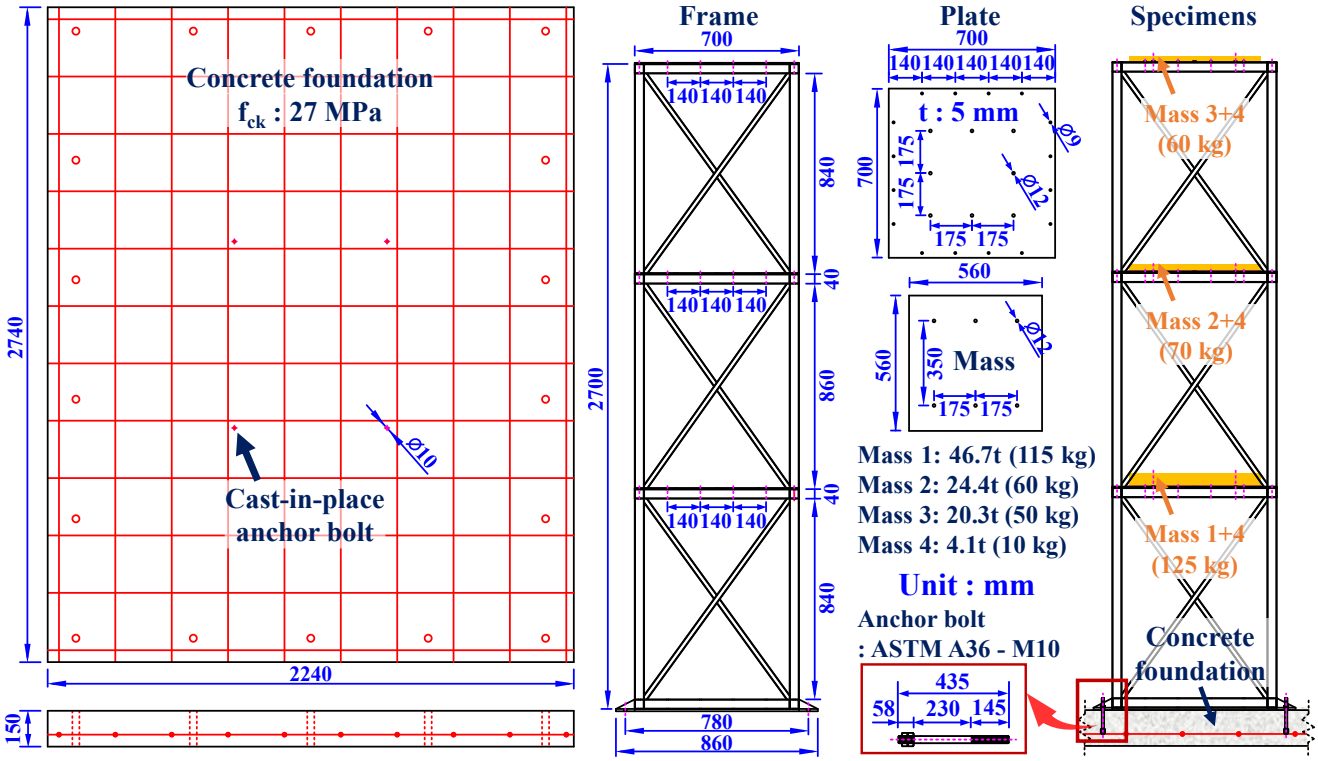


Figure 3. Drawings of specimens.

Table 1. Test results of resonant frequency for safety-related equipment in Korean-type NPPs.

Model Name	Dimensions (mm)			Weight (kg)	Resonant Frequency (Hz)
	Length	Width	Height		
MCC (480 V)	550	1140	2650	1290	20.25 (Side–side) 22.50 (Front–back)
Switchgear (4.16 kV, 50 kA, 1250 A)	2700	1000	2755	4312	8.50 (Side–side) 18.00 (Front–back)
Inverter (40 kVA)	2400	1000	2200	2900	9.00 (Side–side) 23.25 (Front–back)
Battery charger (DC125 V, 600 A)	920	1600	2215	1700	12.25 (Side–side) 29.00 (Front–back)
Load center (480 V)	1600	2000	2480	3750	12.25 (Side–side) 25.00 (Front–back)

2.2. Experimental Setup

2.2.1. Specimen Installation and Setup

Figure 4 illustrates the specimen's installation and configuration for the shaking table test. The electrical cabinet model was assembled by bolting plates and dummy masses for each floor to a frame fabricated from rectangular hollow sections. It was anchored to M10 anchor bolts pre-installed in the concrete foundation, tightened to 400 kgf·cm using a torque wrench [46]. The shaking table tests were conducted using a six-degree-of-freedom shaking table at the Seismic Research and Test Center (SESTEC), an accredited institution in Korea for seismic performance certification of nuclear power plant equipment. The specimen was mounted by rigidly anchoring the concrete foundation directly to the shaking table. Tri-axial accelerometers (PCB Piezotronics models 356A16, 356A17, and 3711B1130G) were installed at the base of the concrete foundation (A1) and on the main vertical frame members of each cabinet floor (A2–A4), as illustrated in Figure 4, to measure acceleration responses.

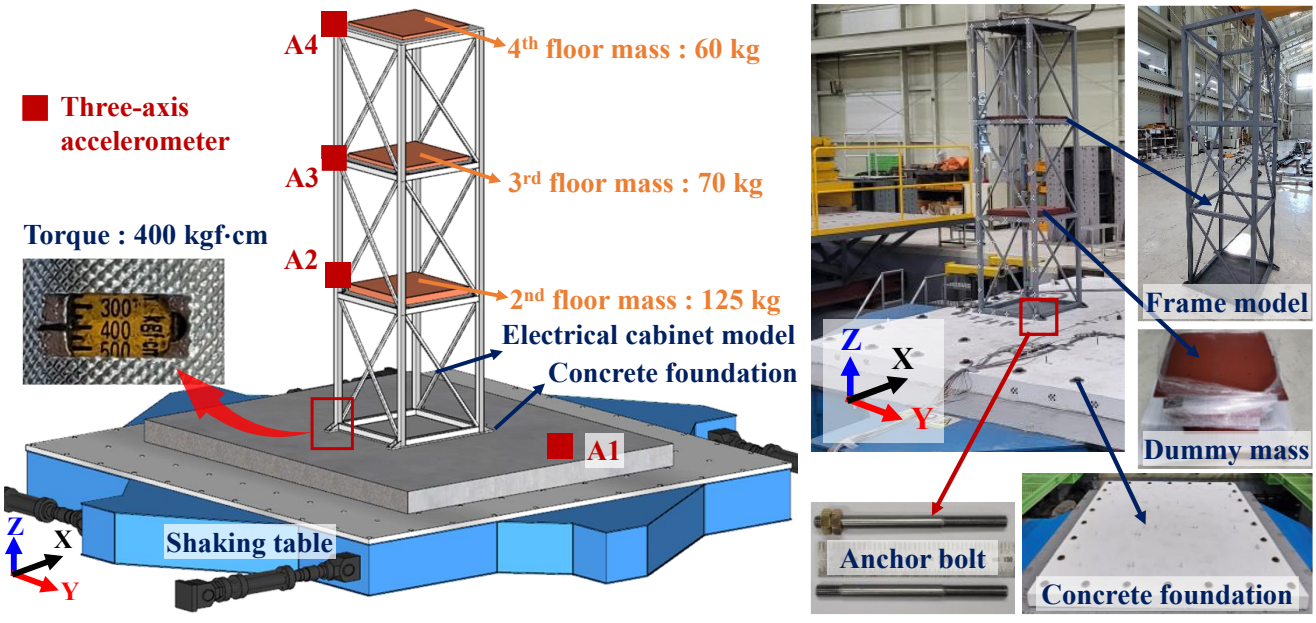


Figure 4. Experimental setup: (**a**) drawings; (**b**) photos.

2.2.2. Input Seismic Motion

The required response spectrum (RRS) for the seismic simulation test is presented in Figure 5. Based on the final safety analysis report of a Korean-type NPP and considering the elevation of the field survey location conducted in this study, the floor response spectra (FRS) at 12.192 m and 21.336 m of the auxiliary building were used to generate the RRS with a damping ratio of 5%. The zero period acceleration (ZPA) was set to 0.2 g in the horizontal directions (X and Y) and 0.14 g in the vertical direction (Z). The acceleration time history was prepared to satisfy the performance capabilities of the shaking table and the requirements of IEEE 344 [47]. It was constructed with a frequency range of 1–50 Hz for 30 s, a strong motion duration of 20 s, and a cross-correlation coefficient not exceeding 0.3, as indicated in Figure 5. In the time history plot (Figure 5), the solid line indicates the acceleration time history generated in accordance with IEEE 344 to match the RRS. In the response spectrum plot, the dashed line indicates the target RRS, while the solid line represents the test response spectrum (TRS) derived from the generated acceleration time history. The shaking table test was conducted to ensure that the TRS adequately enveloped the RRS.

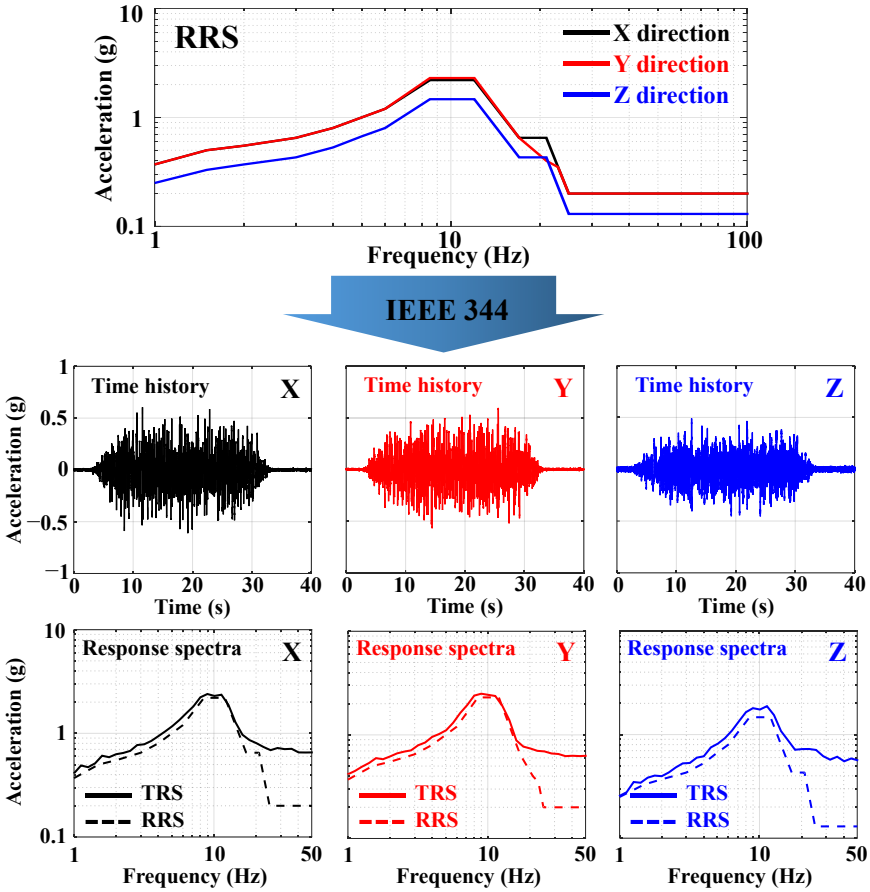


Figure 5. Input seismic motion for seismic simulation test.

2.2.3. Experimental Procedure and Method

This study employed an experimental approach to analyze the seismic behavior of an electrical cabinet model by intentionally inducing support failure to determine the limit state of the specimen. The shaking table test procedure included anomaly checks in sensor signals and visual inspections of the specimen throughout the process. Once the specimen was in a structurally integrity condition, a pre-resonant frequency search test preceded the seismic simulation test. Upon completion, a post-resonant frequency search test was conducted to detect any changes in dynamic characteristics, and a final visual

inspection was carried out to evaluate structural integrity and anchorage conditions. The resonant frequency search test applied random vibration inputs with a root mean square (RMS) value of 0.1 g over a frequency range of 0.5–50 Hz, independently conducted in the horizontal and vertical directions for at least 60 s each. A limit state seismic simulation test was conducted using simultaneous tri-axial excitation, where the input seismic motion was linearly increased from the 100% acceleration level of the RRS, as shown in Figure 5, and continued beyond the onset of damage until specimen failure. If torque loosening of anchor bolts was observed during visual inspection, they were retightened to 400 kgf·cm before further testing. The overall procedure is summarized in Figure 6.

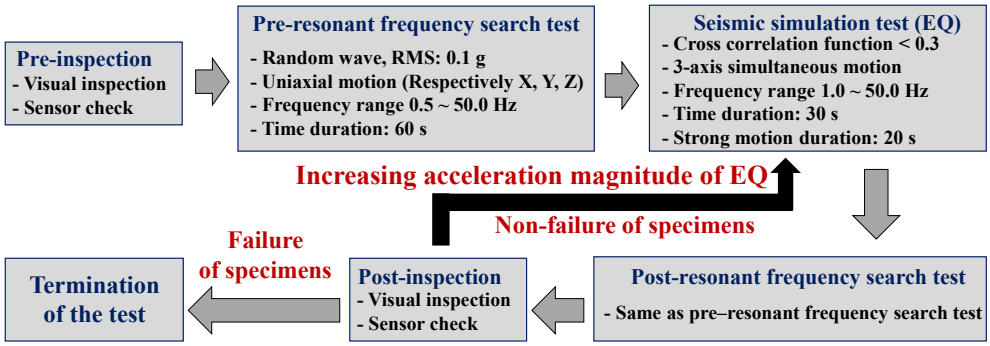


Figure 6. Experimental procedure and method.

2.3. Experimental Results

Table 2 summarizes the results of the visual inspections, which identified damage to the specimen following the resonant frequency search and the limit state seismic simulation tests. The resonant frequency search test is referred to as RES, and the limit state seismic simulation test as EQ throughout this study. The resonant frequency was determined using Equation (1) by deriving the transfer function (T_{ab}), which represents the ratio of the acceleration response at each measurement point to the input acceleration. It is defined as the frequency at which the peak magnitude and the phase angle shift ($\pm 90^{\circ}$) coincide; if they do not, it is defined as the frequency corresponding to the peak magnitude. In this context, P_{aa} denotes the power spectral density of the input signal, and P_{ba} represents the cross power spectral density between the input and output signals.

$$T_{ab}(f) = \frac{P_{ba}(f)}{P_{aa}(f)} \quad (1)$$

Before conducting EQ1, the resonant frequencies of the specimen with maintained structural integrity, measured during RES1, were recorded as 16.75 Hz in the X direction and 15.50 Hz in the Y direction. These values were within the target natural frequency range, indicating that the dynamic characteristics of the specimen appropriately reflected the design of the electrical cabinet model. No structural damage was observed through EQ2. However, during EQ3, two anchor bolts occurred plastic deformation and torque loosening. Approximately 5 mm of plastic deformation was confirmed by comparing the post-test bolt lengths to their original dimensions. The bolts were retightened to the initial torque value, and testing was resumed. RES4, conducted after the observed damage, reduced more resonant frequencies of 1.5%, 8.4%, and 0.6% in the X, Y, and Z directions, respectively, compared to RES1. These changes are graphed in Figure 7. Notably, the frequency variation in the horizontal directions was more than 10 times greater than that in the vertical direction, confirming that the dominant dynamic behavior of the cabinet was governed by global horizontal modes [24,25]. The test was ultimately terminated during

EQ4 due to the failure of three anchor bolts, following the earlier damage. The damage and failure patterns of the specimen are captured in Figure 8.

Table 2. Shaking table test results.

Test ID	Resonant Frequency (Hz) Side–Side (X)	Front–Back (Y)	Vertical (Z)	Remarks (Visual Inspection)
RES1	16.75	15.50	40.50	-
EQ1 (100%)		-		-
RES2	16.75	15.50	40.50	-
EQ2 (200%)		-		-
RES3	16.75	15.25	40.50	-
EQ3 (300%)		-		- Damage to anchor bolts due to plastic deformation (2 units)
RES4	16.50	14.25	40.25	-
EQ4 (350%)		-		- Failure of anchor bolts (3 units) - Termination of the test

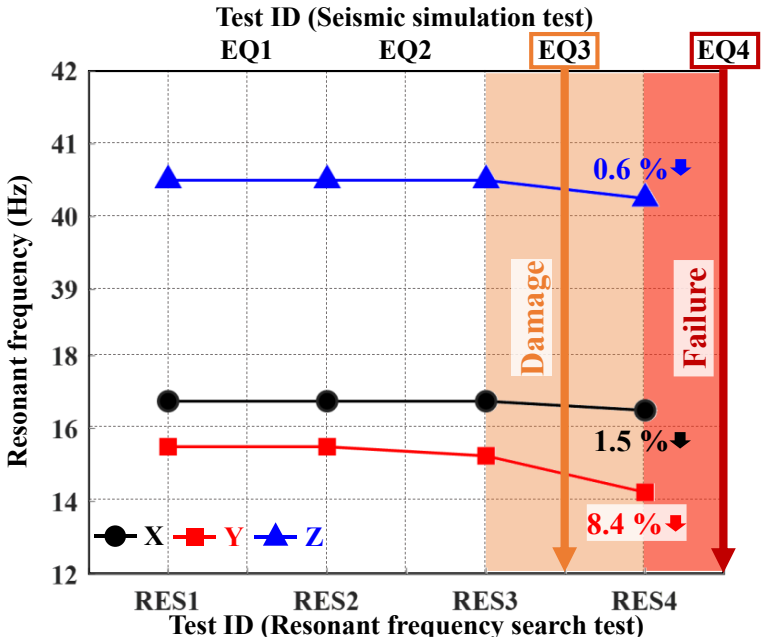


Figure 7. Changes in resonant frequency due to damage.

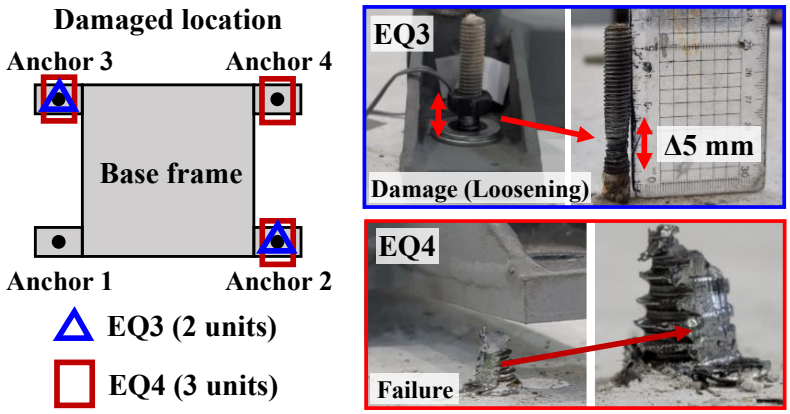


Figure 8. Failure mode of specimens.

3. Numerical Analysis Overview

3.1. Verification of Numerical Model

The electrical cabinet model was fabricated using rectangular hollow sections made of SRT275, following KS D 3568. Table 3 lists the material properties applied in the numerical model. The nonlinear material behavior was modeled using a bi-linear kinematic hardening model, referring to tensile test results from previous studies, as illustrated in Figure 9 [48,49].

Table 3. Material properties (SRT275).

Density (ton/mm^3)	Young's Modulus (MPa)	Poisson's Ratio	Yield Stress (MPa)	Plastic Strain
7.85×10^{-9}	210,000	0.3	395.69 467.00	0 0.198

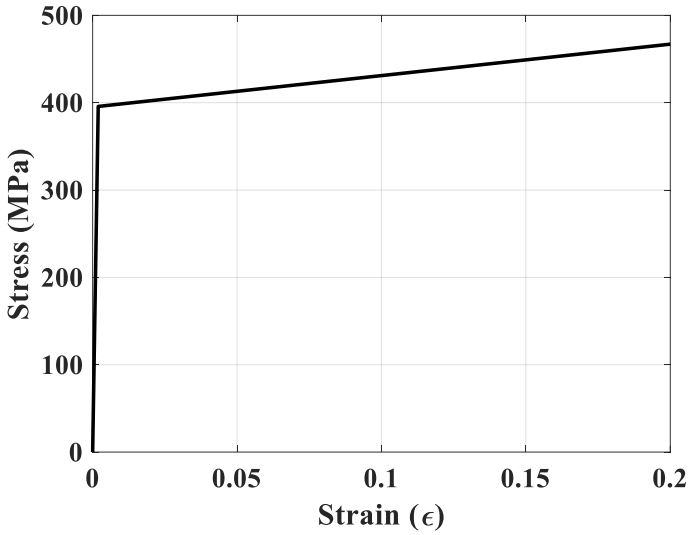


Figure 9. Bi-linear kinematic hardening model [48,49].

The dimensions of the rectangular hollow sections used for the main members of the electrical cabinet model differed from the nominal values specified in KS D 3568 due to discrepancies in actual production. Accordingly, the fabricated specimen was physically measured, and the corresponding dimensions in the preliminary numerical model were updated to reflect these measurements. The electrical cabinet model's frame—constructed by welding columns, beams, and braces—was partitioned and merged into a single part. The connections between the frame and the plates were modeled using tie constraints. Dummy masses, bolted onto the plates at each floor, were defined as nonstructural mass and applied directly to the plates. All parts were modeled using solid elements with hexahedral meshing (C3D8R), which employ linear reduced integration. The mesh size of the numerical model was set to 20 mm, which was sufficiently small to ensure convergence without significant differences in the analysis results. The final numerical model comprised 52,071 elements and 94,384 nodes, as detailed in Figure 10. A 3% damping ratio was defined in accordance with NUREG/CR-6919 and implemented using Rayleigh damping [50]. The applied Rayleigh damping coefficients were $\alpha = 3.022$ and $\beta = 0.000297$. The anchorage boundary condition was modeled as a fixed support, constraining displacements in tri-axial directions. The mesh in the anchor bolt connection region was locally refined to optimize the numerical model.

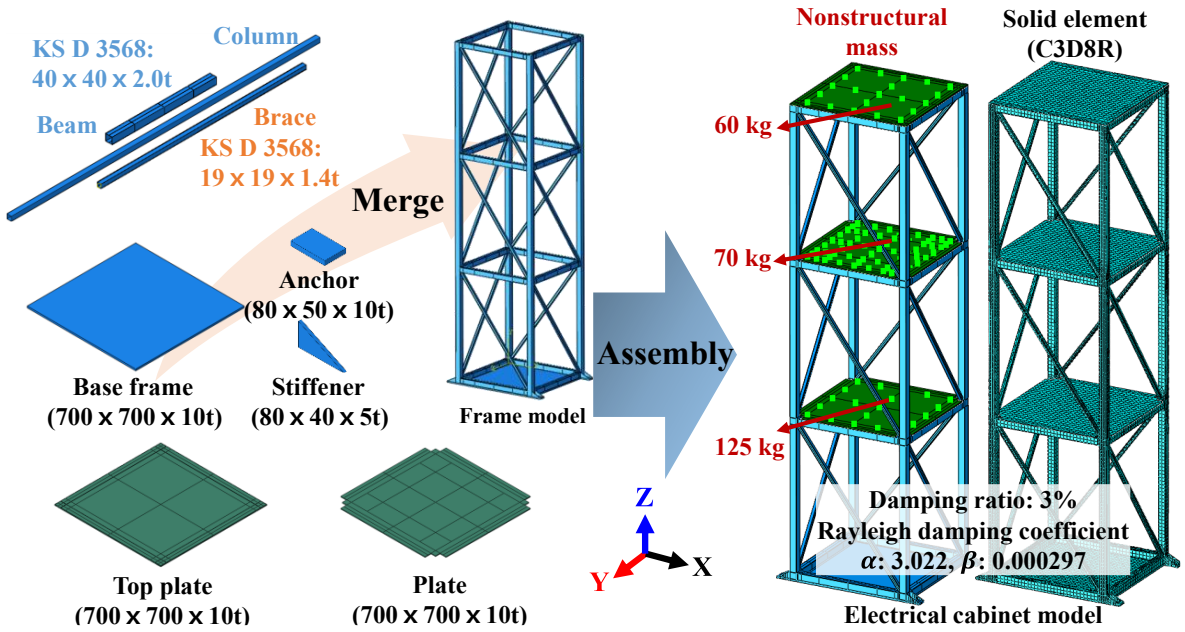


Figure 10. Optimized numerical model.

An eigenvalue analysis was performed to validate the optimized numerical model's accuracy. The resulting mode shapes are presented in Figure 11, with the corresponding translational and rotational participation factors for each mode summarized in Table 4. The natural frequencies of the first and second modes were found to be 15.18 Hz and 16.99 Hz, respectively. For the first mode, the participation factors were 0.855 (Y-direction translation) and 0.969 (X-direction rotation); for the second mode, they were 0.951 (X-direction translation) and 0.970 (Y-direction rotation), with rotational components dominating. This result aligns with the shaking table test findings, confirming that the dominant global modes of the cabinet are characterized by bending behavior in the two horizontal directions [23,24]. As shown in Table 5, the numerical model weighed 410.73 kg, closely matching the specimen's 410.00 kg (0.18% difference). Natural frequencies varied by 2.12% and 1.43% from experimental results. The percentage difference (PD) used was calculated using Equation (2), with V_1 and V_2 representing the values obtained from the specimen and the numerical model, respectively, for calculating the percentage difference between experimental and numerical results. The natural frequency differences remained within 1–2%, and the weight difference was under 1%, confirming the developed numerical model's accuracy in simulating the specimen.

Table 4. Modal participation factors.

Mode	Translation			Rotation		
	X	Y	Z	X	Y	Z
1	0.002	0.855	0.000	0.969	0.000	0.403
2	0.951	0.001	0.000	0.000	0.970	0.334

Table 5. Validation of the numerical model.

	Type	Mode 1 (Y)	Mode 2 (X)	Weight (kg)
Specimen	Resonant frequency (Hz)	15.50	16.75	410.00
Numerical model	Natural frequency (Hz)	15.18	16.99	410.73
	PD (%)	2.12	1.43	0.18

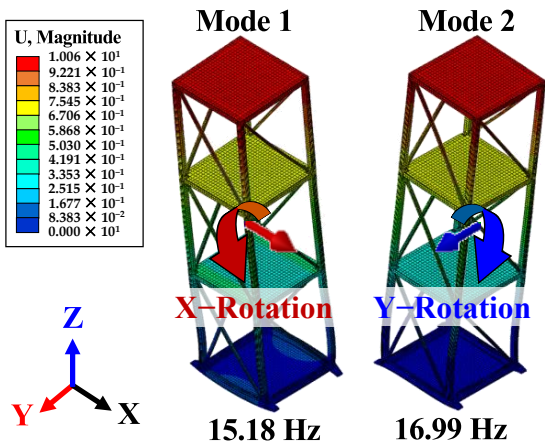


Figure 11. Mode shape of numerical model.

$$\text{Percentage difference}(\%) = \frac{|V_1 - V_2|}{(V_1 + V_2)/2} \quad (2)$$

3.2. Seismic Response Analysis

During the shaking table test, anchor bolt failure occurred at EQ4 (350%), terminating the test due to the cessation of excitation. Accordingly, comparisons between the experimental and numerical results were limited to EQ1 through EQ3, prior to the onset of anchor bolt failure. Figure 12 details the displacement time histories corresponding to the shaking table feedback motion for each EQ. Seismic response analysis was performed on the numerical model by applying the displacement time histories corresponding to each EQ in Figure 12, which were used as input seismic motions in the shaking table tests. As described in Figure 13, acceleration responses were extracted from the nodes corresponding to the locations of the accelerometers installed on the specimen. Differences in the seismic behavior characteristics of the electrical cabinet model were evaluated by comparing the acceleration response results obtained from the seismic response analysis and the shaking table test.

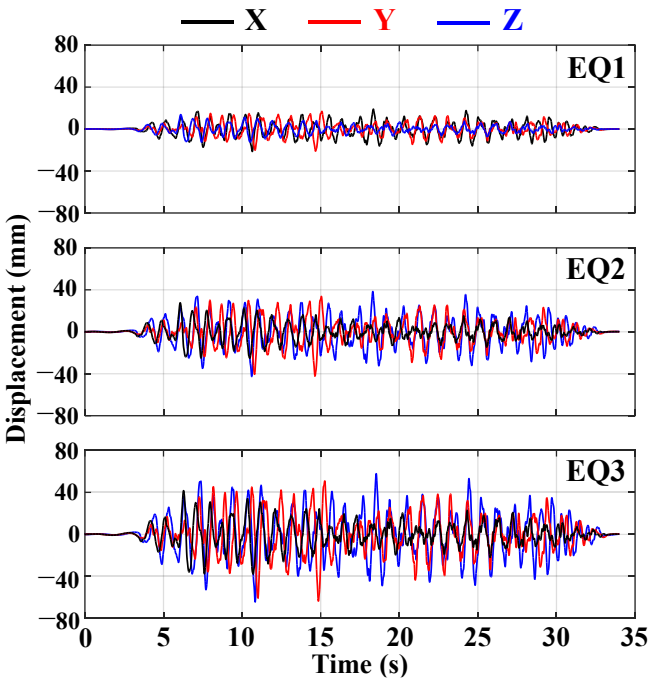


Figure 12. Input seismic motion for seismic response analysis.

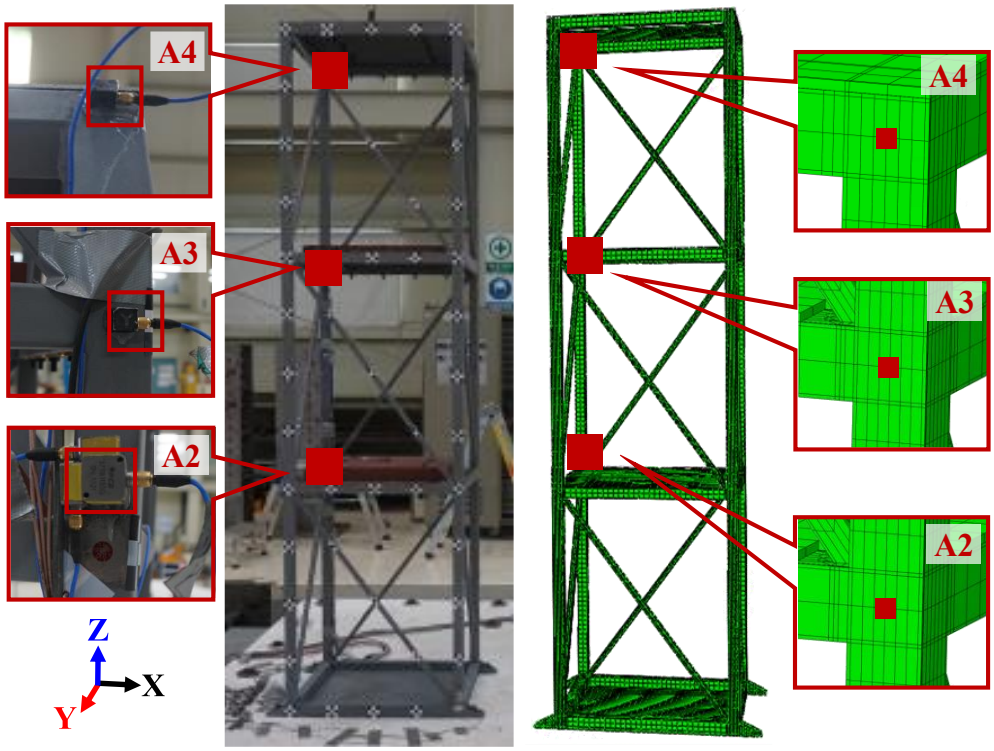


Figure 13. Location of output nodes for response comparison.

4. Analysis and Comparison of Results

4.1. Comparison of Acceleration Response Time Histories

The acceleration response time histories obtained from the experimental and numerical results for EQ1 through EQ3 are presented in Figures 14–16, for each axial direction at locations A2 to A4. As drawn in Figure 14, the acceleration time histories from the experimental and numerical results under EQ1 exhibited a high degree of similarity. The responses showed close agreement in both horizontal and vertical directions as well as across the full height of the electrical cabinet model, confirming the validity of the numerical model. Although no structural damage was observed at EQ2, minor impact responses began to appear, specifically at the upper levels of the cabinet, as depicted in Figure 15. These responses are attributed to the increased seismic input. At EQ3, where damage occurred due to plastic deformation of the anchor bolts, significant amplification of the acceleration responses and multiple impact signals were observed (Figure 16). In particular, the vertical (Z) direction exhibited numerous noise-like signals, likely caused by substantial impact events. To quantify the similarity between the acceleration responses from the experimental and numerical results, cross-correlation coefficients were calculated, as outlined in Table 6. The coefficient ranges from –1 to 1, with values closer to ± 1 indicating higher similarity, and 1 denoting identical signals. At EQ1, the cross-correlation coefficients ranged from 0.912 to 0.978 in the horizontal directions and from 0.675 to 0.726 in the vertical direction. Notably, the horizontal directions—representing the dominant dynamic behavior of the cabinet—showed strong agreement with coefficients exceeding 0.912. As the input seismic motion increased, the variability in correlation across different elevations also increased. At EQ3, the coefficients significantly declined, ranging from 0.638 to 0.832 in the horizontal directions and from 0.506 to 0.605 in the vertical direction.

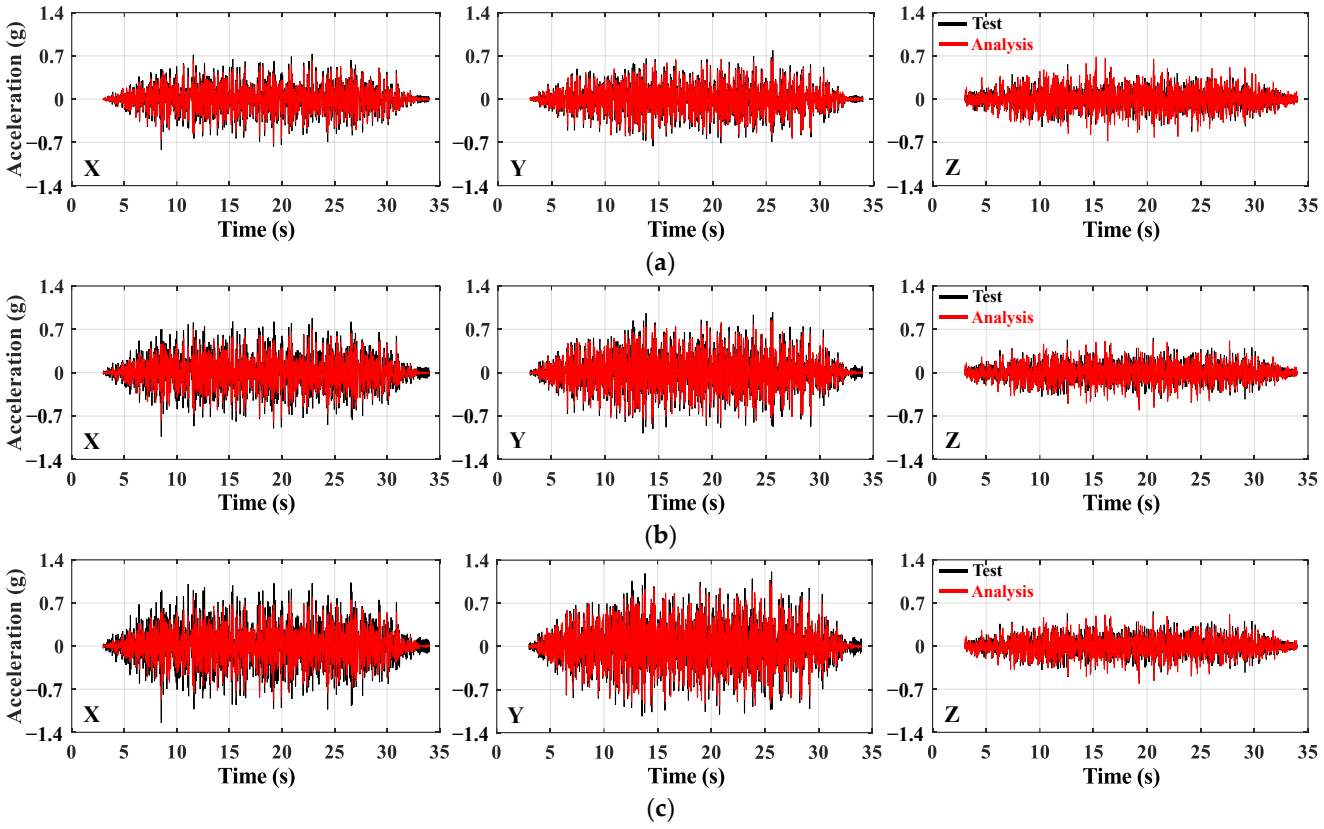


Figure 14. Comparison of acceleration response time histories (EQ1): (**a**) A2; (**b**) A3; (**c**) A4.

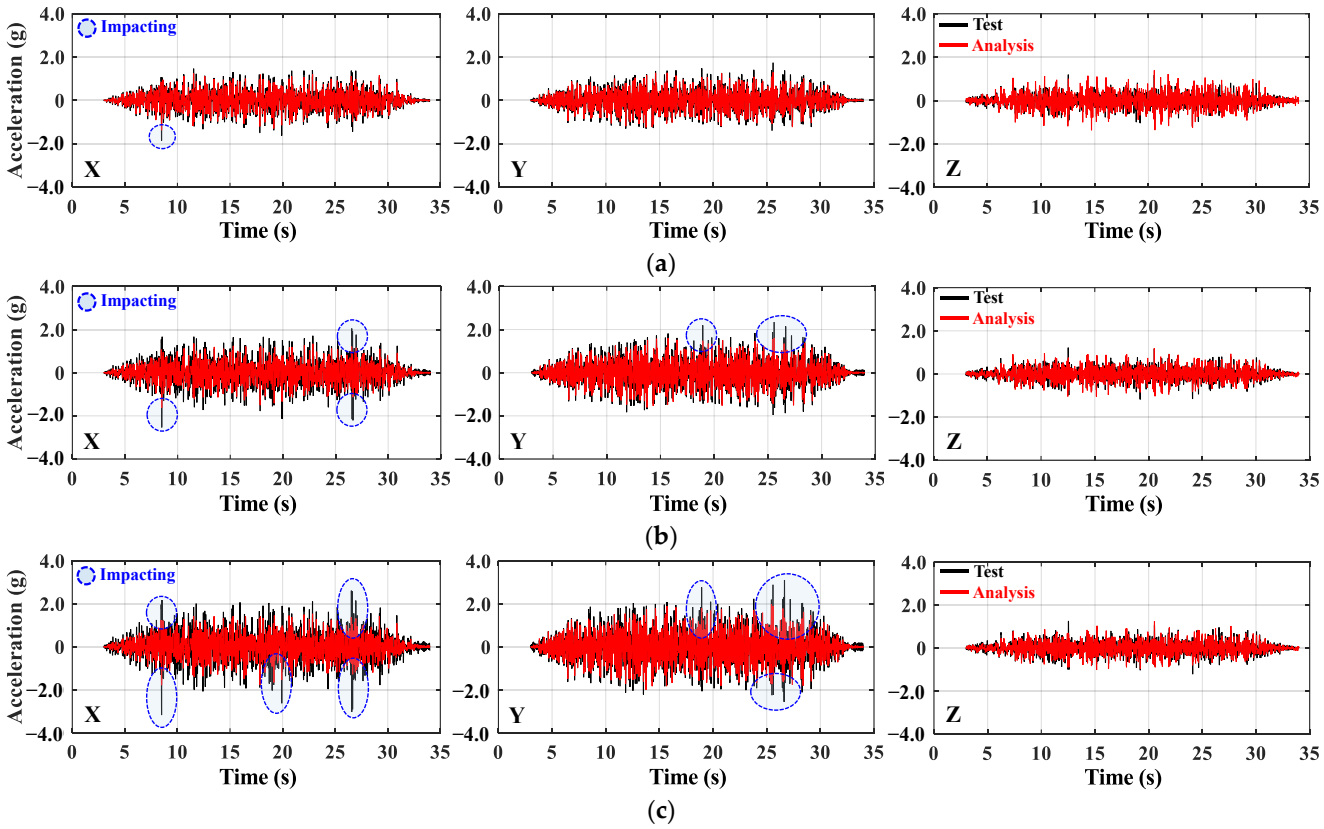


Figure 15. Comparison of acceleration response time histories (EQ2): (**a**) A2; (**b**) A3; (**c**) A4.

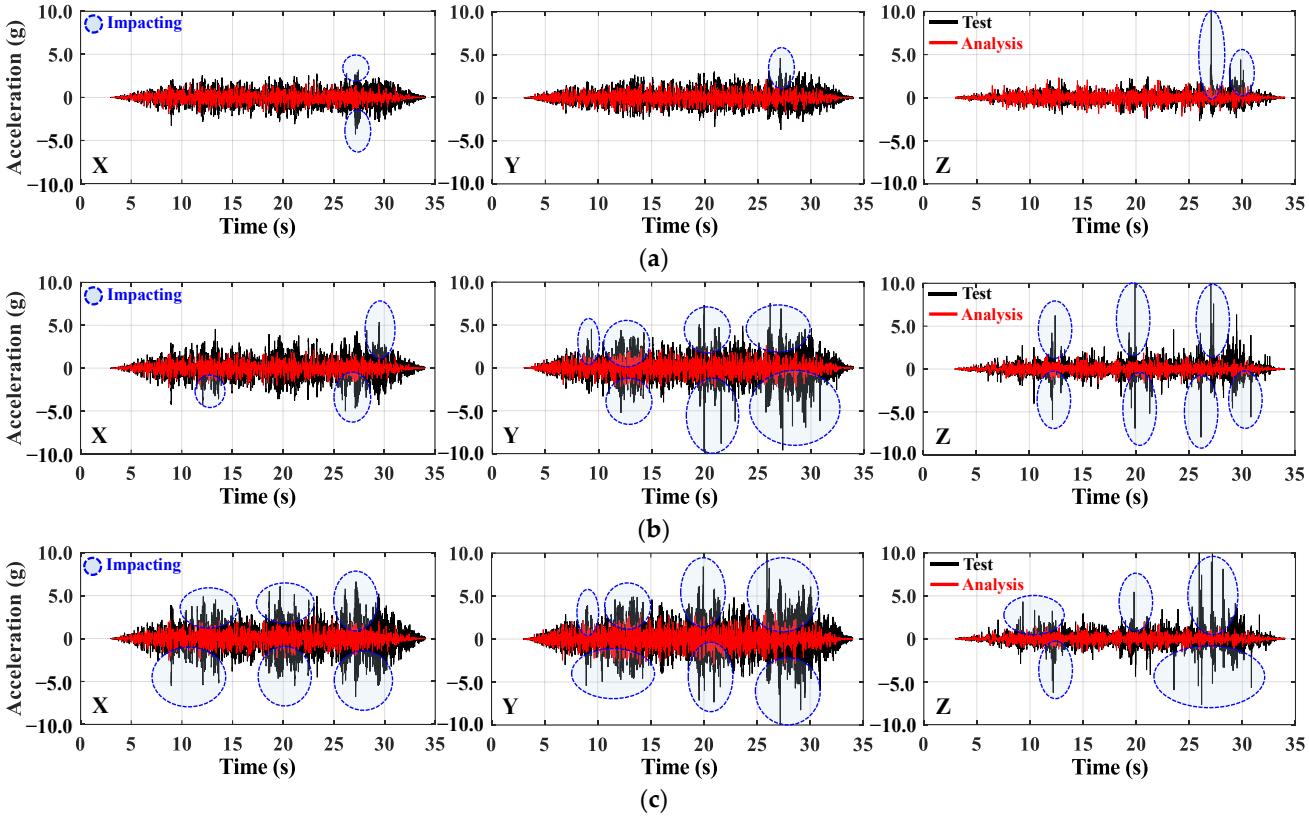


Figure 16. Comparison of acceleration response time histories (EQ3): (**a**) A2; (**b**) A3; (**c**) A4.

Table 6. Cross-correlation coefficients of acceleration responses between experimental and numerical results.

Location	Direction	Test ID		
		EQ1	EQ2	EQ3
A2	X	0.975	0.957	0.811
	Y	0.978	0.973	0.832
	Z	0.675	0.761	0.605
A3	X	0.945	0.906	0.722
	Y	0.963	0.951	0.737
	Z	0.726	0.801	0.549
A4	X	0.912	0.855	0.638
	Y	0.950	0.936	0.725
	Z	0.717	0.785	0.506

RMS, a representative measure of the effective amplitude of a time history signal independent of frequency, is widely used to quantitatively assess the acceleration response of electrical equipment [8,51]. In addition, root mean quad (RMQ) can serve as a more sensitive indicator when the signal contains impacts or irregularities, making it useful in capturing impulsive characteristics [52]. To compare the seismic behavior between the experimental and numerical results, RMS and RMQ values were computed using Equations (3) and (4) to quantify the magnitude of acceleration response signals. Based on these values, the RMS ratio (R_{RMS}) and RMQ ratio (R_{RMQ}) were calculated using Equation (5) to evaluate amplitude amplification according to the cabinet's height.

$$\mathrm{RMS} = \sqrt{\frac{1}{n}\sum_{k=1}^{n} x_k^2} \tag{3}$$

$$\mathrm{RMQ} = \sqrt[4]{\frac{1}{n}\sum_{k=1}^{n} x_k^4} \tag{4}$$

$$\mathrm{R_{RMS}}(i) = \frac{\mathrm{RMS}_a(\mathrm{floor})}{\mathrm{RMS}_a(\mathrm{base})}, \mathrm{R_{RMQ}}(i) = \frac{\mathrm{RMQ}_a(\mathrm{floor})}{\mathrm{RMQ}_a(\mathrm{base})} \tag{5}$$

In Equations (3) and (4), x_k represents the k-th value of the measured time history signal, and n is the total number of samples. In Equation (5), $\mathrm{RMS}_a(\mathrm{floor})$ and $\mathrm{RMQ}_a(\mathrm{floor})$ denote the RMS and RMQ values at each cabinet floor (A2–A4), and $\mathrm{RMS}_a(\mathrm{base})$ and $\mathrm{RMQ}_a(\mathrm{base})$ values at the shaking table base (A1). Tables 7 and 8 present RMS and $\mathrm{R_{RMS}}$ values, as well as RMQ and $\mathrm{R_{RMQ}}$ values, from the experimental and numerical results. Figure 17 shows RMS and RMQ differences, while Figure 18 depicts $\mathrm{R_{RMS}}$ and $\mathrm{R_{RMQ}}$ differences. In Figure 17, black and red indicate experimental and numerical results; circles and squares denote RMS and RMQ, respectively. As specified in Figure 17a, the RMQ difference for EQ1 reached a maximum of 13.23% at the top of the electrical cabinet model (A4), whereas differences in RMS and RMQ at other positions and directions ranged from 0.08% to 12.10%. Similarly, previous studies on numerical modeling postulate that discrepancies of less than 15% between numerical and experimental results are considered reasonable and reliable, indicating that the acceleration response magnitudes for EQ1 are in good agreement between the numerical and experimental results [53–55]. Prior to EQ3 (Figure 17a,b), differences in RMS and RMQ increase linearly with cabinet height, with RMQ variations consistently larger than RMS. For EQ3 (Figure 17c), RMS differs by up to 49.95% (X-direction) and RMQ by 58.81%. Discrepancies between the experimental and numerical results in EQ3 are significantly greater than those found in EQ1 and EQ2 across all locations and directions, with RMQ exhibiting greater variability than RMS. Unlike the trend observed in EQ1 and EQ2—where variations were more pronounced in the horizontal directions (X and Y) than in the vertical (Z)—EQ3 showed a reversal, with the largest variation occurring in the vertical direction, reaching up to 87.24%. Figure 18 shows the experimental results in black and the numerical results in red. Data points corresponding to the X, Y, and Z directions are represented by circle, square, and triangle markers, respectively. $\mathrm{R_{RMS}}$ increased linearly with height as input seismic motion increased (Figure 18a). In Figure 18b, $\mathrm{R_{RMQ}}$ was greater than $\mathrm{R_{RMS}}$ and was higher at A2 than at A3. Figure 19 describes $\mathrm{R_{RMS}}$ and $\mathrm{R_{RMQ}}$ differences at A4, where the trend of acceleration response amplification was most evident. The figure clarifies the variation in directional differences as the input seismic motion increases. $\mathrm{R_{RMQ}}$ differences exceeded $\mathrm{R_{RMS}}$ across all directions, and notably, in EQ3, RMQ differences in the vertical direction surpassed those in the horizontal direction. Accordingly, the $\mathrm{R_{RMS}}$ values obtained from the experimental results increased linearly with height along all three axes as the input seismic motion increased, whereas the $\mathrm{R_{RMQ}}$ values showed greater amplification in the vertical direction and exhibited a nonlinear trend along the height of the electrical cabinet model.

While cabinet response amplification generally increases with height, RMQ analysis revealed that internal impacts can cause the peak amplification to occur at any location previously discussed in [31]. Furthermore, calculating RMS and RMQ from the acceleration time history responses confirmed that the differences in seismic behavior of the electrical cabinet between the experimental and numerical results effectively capture the effects of anchorage damage and impulsive characteristics.

Table 7. Calculation results for RMS and R_{RMS}.

Type		Location	EQ1 X	EQ1 Y	EQ1 Z	EQ2 X	EQ2 Y	EQ2 Z	EQ3 X	EQ3 Y	EQ3 Z
A1			0.160	0.153	0.114	0.314	0.303	0.249	0.455	0.439	0.382
RMS (g)	Test	A2	0.205	0.207	0.136	0.406	0.421	0.261	0.716	0.763	0.498
		A3	0.254	0.268	0.132	0.517	0.559	0.258	1.002	1.174	0.583
		A4	0.302	0.323	0.133	0.631	0.692	0.267	1.328	1.501	0.620
	Analysis	A2	0.206	0.200	0.144	0.415	0.405	0.300	0.604	0.593	0.453
		A3	0.241	0.261	0.132	0.480	0.527	0.274	0.699	0.776	0.412
		A4	0.275	0.319	0.133	0.545	0.642	0.273	0.797	0.950	0.408
R_{RMS} (g/g)	Test	A2	1.289	1.307	1.260	1.323	1.337	1.205	1.329	1.352	1.188
		A3	1.507	1.705	1.153	1.529	1.740	1.100	1.536	1.767	1.079
		A4	1.716	2.080	1.159	1.738	2.122	1.095	1.752	2.165	1.068
	Analysis	A2	1.278	1.352	1.187	1.296	1.391	1.047	1.574	1.738	1.304
		A3	1.584	1.747	1.152	1.649	1.848	1.036	2.201	2.673	1.526
		A4	1.885	2.112	1.162	2.010	2.286	1.072	2.919	3.419	1.625
PD (%)		A2	0.84	3.38	5.98	2.08	3.94	14.03	16.91	25.01	9.32
		A3	4.97	2.41	0.08	7.54	6.02	5.94	35.63	40.84	34.29
		A4	9.39	1.55	0.25	14.52	7.47	2.14	49.95	44.91	41.34

Table 8. Calculation results for RMQ and R_{RMQ}.

Type		Location	EQ1 X	EQ1 Y	EQ1 Z	EQ2 X	EQ2 Y	EQ2 Z	EQ3 X	EQ3 Y	EQ3 Z
A1			0.224	0.214	0.160	0.442	0.423	0.356	0.644	0.615	0.547
RMQ (g)	Test	A2	0.286	0.288	0.188	0.575	0.584	0.371	1.036	1.084	1.351
		A3	0.352	0.372	0.183	0.737	0.777	0.368	1.456	1.798	1.346
		A4	0.419	0.450	0.184	0.908	0.966	0.378	1.940	2.210	1.512
	Analysis	A2	0.275	0.274	0.212	0.550	0.543	0.452	0.800	0.797	0.702
		A3	0.322	0.355	0.189	0.634	0.705	0.394	0.925	1.039	0.605
		A4	0.367	0.431	0.192	0.722	0.857	0.392	1.058	1.274	0.593
R_{RMQ} (g/g)	Test	A2	1.227	1.279	1.327	1.243	1.286	1.269	1.242	1.296	1.283
		A3	1.433	1.658	1.185	1.433	1.666	1.106	1.435	1.691	1.106
		A4	1.633	2.014	1.201	1.633	2.027	1.101	1.643	2.072	1.085
	Analysis	A2	1.273	1.348	1.175	1.301	1.381	1.040	1.607	1.762	2.470
		A3	1.567	1.740	1.147	1.666	1.838	1.032	2.260	2.924	2.461
		A4	1.865	2.102	1.153	2.054	2.284	1.062	3.011	3.594	2.763
PD (%)		A2	3.73	5.27	12.10	4.53	7.16	19.82	25.65	30.49	63.28
		A3	8.89	4.84	3.21	15.04	9.79	6.91	44.67	53.44	75.99
		A4	13.23	4.25	4.02	22.82	11.96	3.65	58.81	53.74	87.24

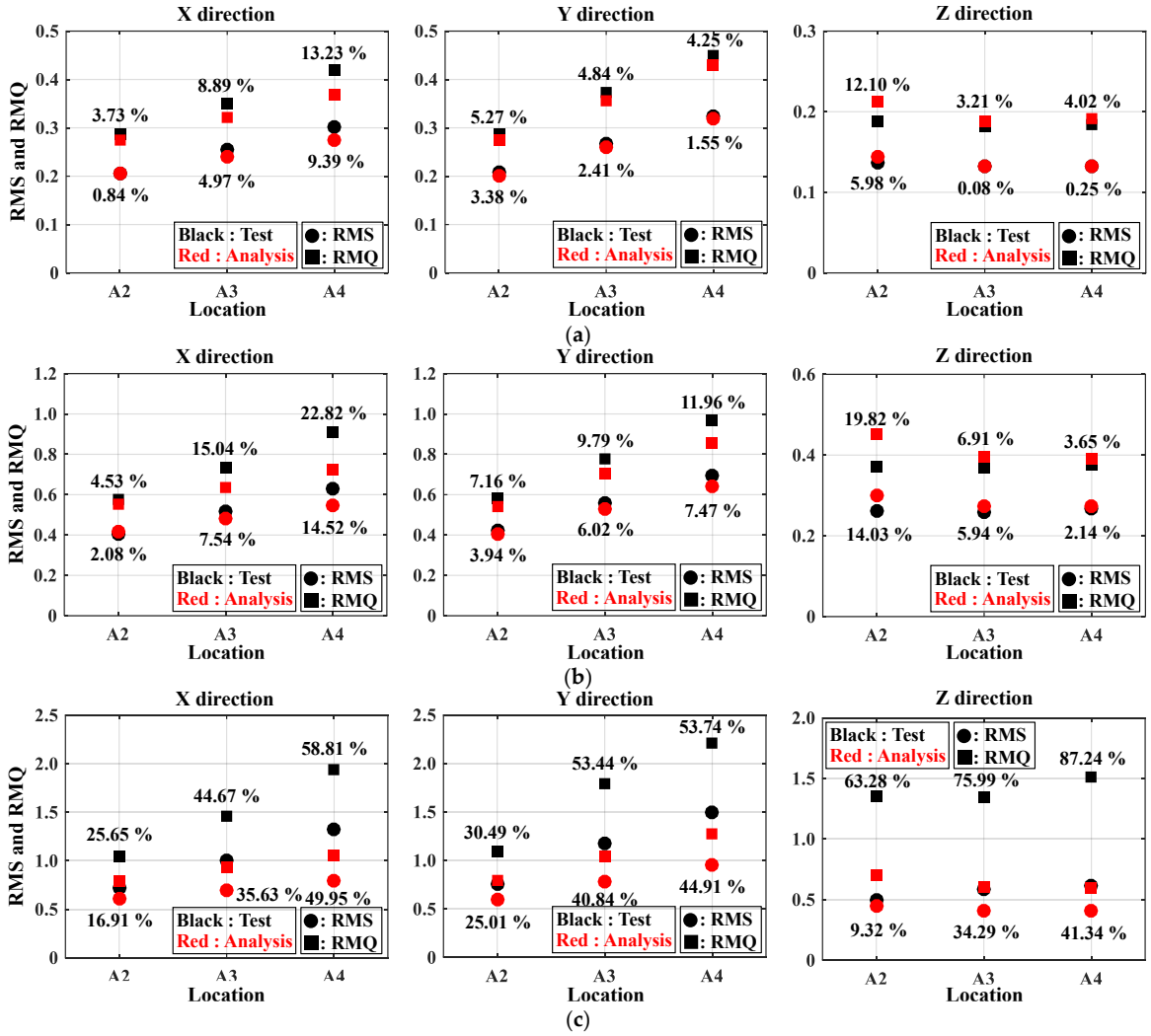


Figure 17. Comparison of RMS and RMQ: (**a**) EQ1; (**b**) EQ2; (**c**) EQ3.

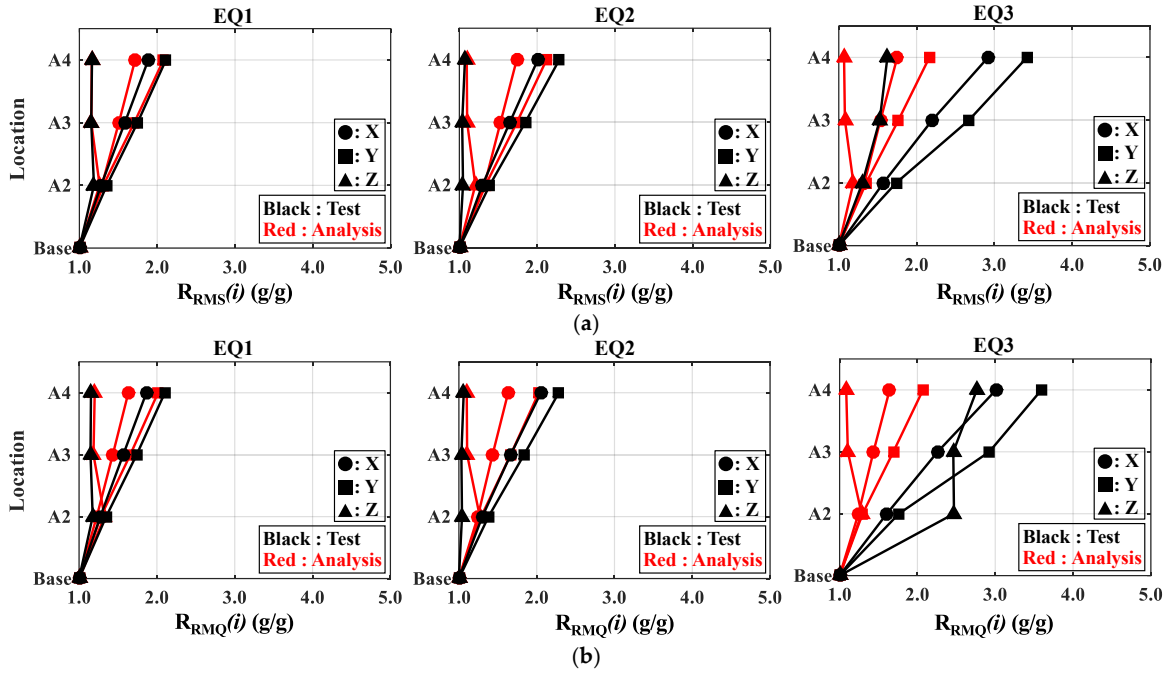


Figure 18. Comparison of RMS ratio and RMQ ratio: (**a**) R_{RMS}; (**b**) R_{RMQ}.

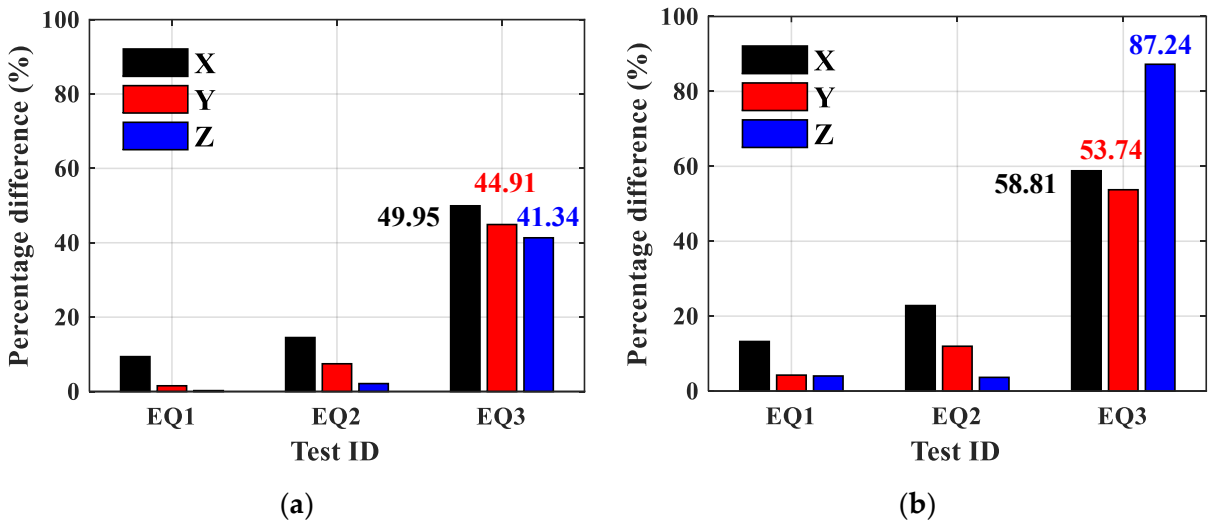


Figure 19. Percentage difference of RMS ratio and RMQ ratio in A4: (**a**) R_{RMS}; (**b**) R_{RMQ}.

4.2. Comparison of Acceleration Response Spectra

FRS were calculated at locations A2 to A4 in each axial direction from the acceleration response time history to analyze and compare the seismic behavior of the electrical cabinet model between the experimental and numerical results. These were then analyzed using a damping ratio of 5% and a 1/12 octave bandwidth. Figures 20–22 present the FRS results along with those of the input seismic motion: black lines indicate the experimental results, red the numerical results, and blue the input seismic motion. In EQ1 (Figure 20), the experimental and numerical results had good agreement across all three directions. The FRS increased with height, particularly in the resonant frequency range of the horizontal directions (X and Y). In EQ2 (Figure 21), where no damage occurred despite increased input seismic motion, the experimental FRS exhibited greater amplification than the numerical FRS. While the vertical FRS remained consistent with the input seismic motion, the horizontal FRS exhibited notable amplification within the resonant frequency range, excluding low- and high-frequency ranges. Results from EQ1 and EQ2 demonstrated that amplification within the resonant frequency range generally increases with height. As represented in Figure 22, for EQ3—where damage occurred to the specimen—the experimental FRS showed greater amplification variations than the numerical FRS in the horizontal directions within the resonant frequency range. Moreover, the experimental FRS exhibited significant amplification across all three axes in the high-frequency range. Notably, whereas high-frequency amplification in the horizontal directions had increased gradually with input seismic motion, the vertical direction showed a sharp increase only during EQ3. Since global horizontal modes govern the cabinet's dynamic behavior, horizontal responses increased linearly with seismic motion in most frequency ranges, excluding low-frequency ranges. However, anchorage damage and impact effects contributed substantially to high-frequency and vertical amplification. These findings align with NUREG CR-5203, stating that vertical excitation rarely amplifies low frequencies but strongly affects high frequencies due to local modes and impacts [31].

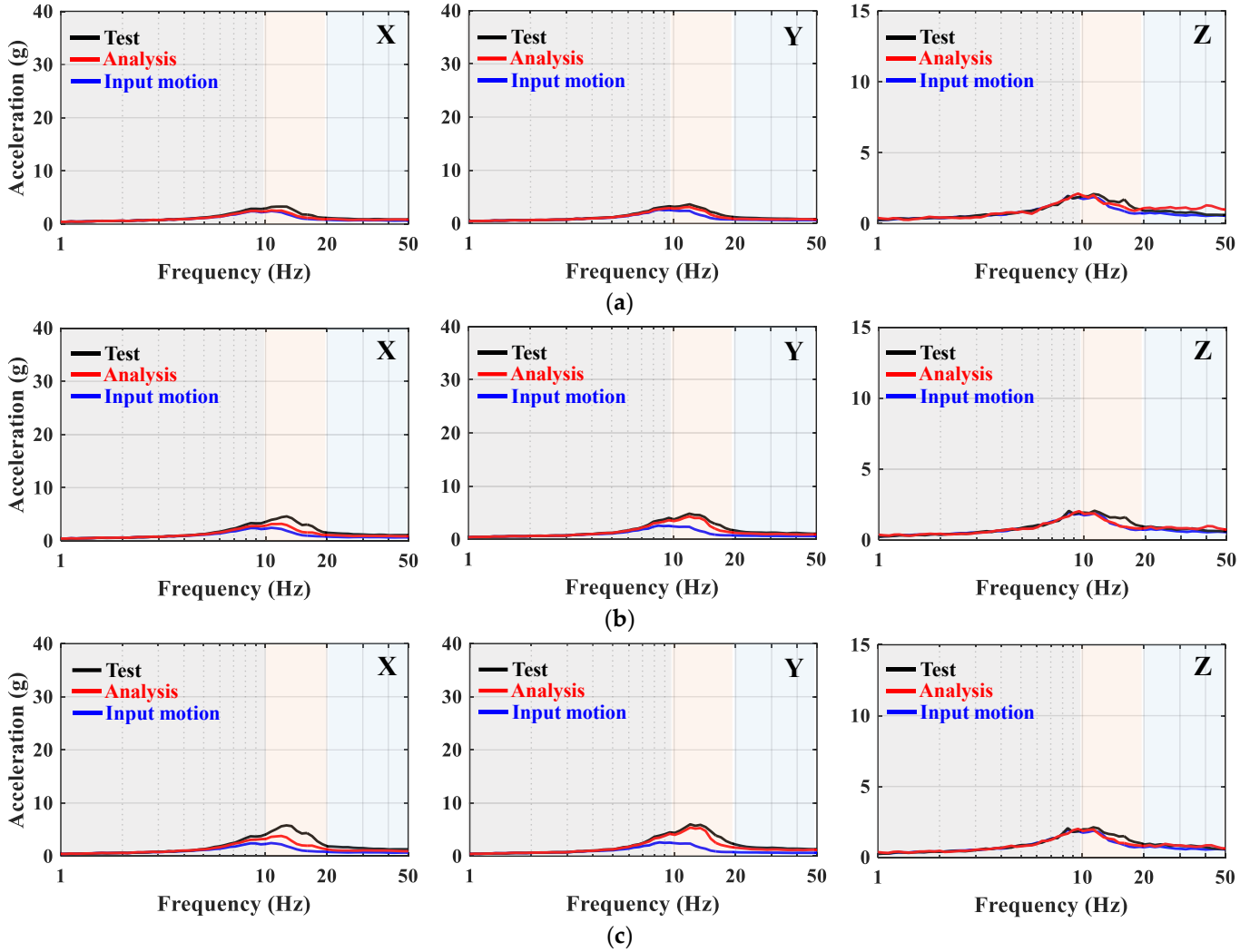


Figure 20. Comparison of FRS (EQ1): (**a**) A2; (**b**) A3; (**c**) A4.

Simply comparing the peak values of FRS may not be sufficient to evaluate the dynamic characteristics of electrical equipment under seismic loading. According to IEEE Std 693, ZPA represents the maximum acceleration in the high-frequency range beyond the RRS [56]. This study defined ZPA based on the highest frequency of the RRS and the performance capacity of the shaking table. Considering the shaking table's performance and the FRS octave bandwidth, the spectral acceleration at 45.25 Hz was adopted as the ZPA [10]. Additionally, using average and peak values within defined frequency ranges offers a practical means of evaluating acceleration amplification [31,57]. However, if the frequency range is set too broadly, these values may be distorted and misrepresent actual system behavior. Thus, defining an appropriate frequency range is essential. Three frequency ranges were defined in this study for calculating average and peak values based on the frequency content of the input seismic motion and the cabinet's resonant frequencies: 1–10 Hz (low frequency), 10–20 Hz (resonant frequency), and 20–50 Hz (high frequency). According to Equation (6), the amplification ratios of the average value (R_{Avg}), peak value (R_{Peak}), and ZPA (R_{ZPA}) were calculated for each defined frequency range and are summarized in Tables 9–11. As in Equation (5), these ratios indicate the response at each cabinet floor level (A2–A4) relative to the shaking table base (A1). Their comparison is shown in Figure 23. Figure 23a,b use black, red, and blue to indicate low, resonant, and high-frequency ranges, respectively, with circle, square, and triangle markers denoting X, Y, and Z directions, respectively. The solid lines represent experimental results, and

the dashed lines signify numerical results. In Figure 23c, black indicates the experimental results and red indicates the numerical results, with circle, square, and triangle markers representing the X, Y, and Z directions, respectively. As in previous comparisons, the experimental results generally showed higher amplification than the numerical results across all three methods. Amplification ratios were higher at EQ3 than at EQ1 and EQ2. Notably, while R_{ZPA} was lower than R_{Avg} and R_{Peak} in EQ1 and EQ2, it exceeded both in EQ3. The increase in amplification with cabinet height and seismic motion was generally linear. As illustrated in Figure 23c, the R_{ZPA} measured at EQ3 exhibits somewhat more irregular and nonlinear behavior with respect to height compared to R_{Avg} and R_{Peak}. In Figure 23a,b, R_{Avg} and R_{Peak} result in similar trends at EQ1 and EQ2; however, in the high-frequency range of EQ3, R_{Peak} is relatively larger than R_{Avg}. As shown in Figure 22, in the resonant frequency range of 10–20 Hz, the acceleration response is uniformly amplified, resulting in relatively similar values for R_{Avg} and R_{Peak}. In contrast, in the high-frequency range, acceleration amplification increases rapidly with frequency, causing R_{Peak} to exceed R_{Avg}. Since the R_{ZPA} corresponds to a high frequency of 45.25 Hz, it exhibited a pattern similar to that of R_{Peak} in the high-frequency range.

$$R_{Avg}(i) = \frac{\text{Average}_a(\text{floor})}{\text{Average}_a(\text{base})}, \qquad R_{Peak}(i) = \frac{\text{Peak}_a(\text{floor})}{\text{Peak}_a(\text{base})}, \qquad R_{ZPA}(i) = \frac{\text{ZPA}_a(\text{floor})}{\text{ZPA}_a(\text{base})} \tag{6}$$

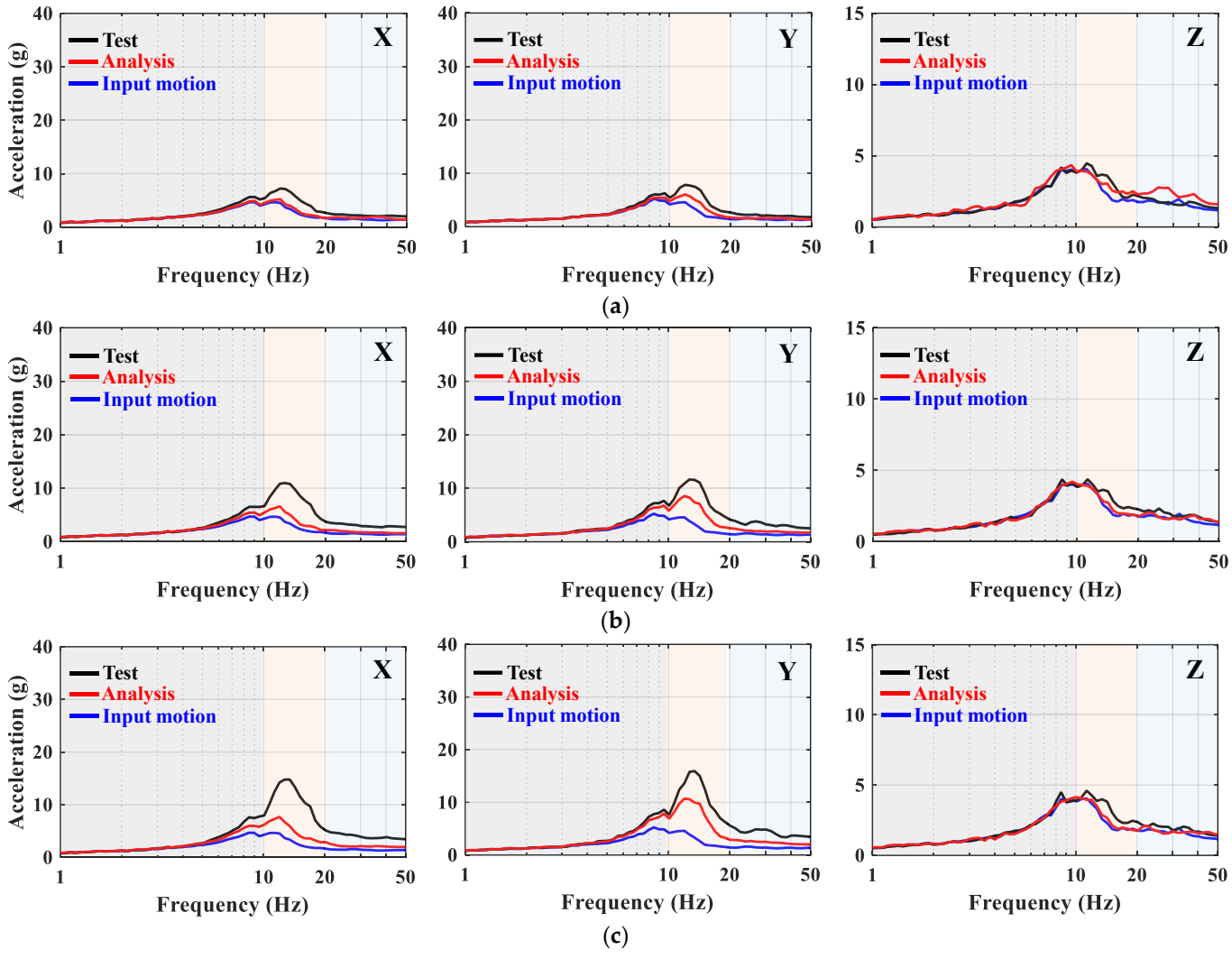


Figure 21. Comparison of FRS (EQ2): (**a**) A2; (**b**) A3; (**c**) A4.

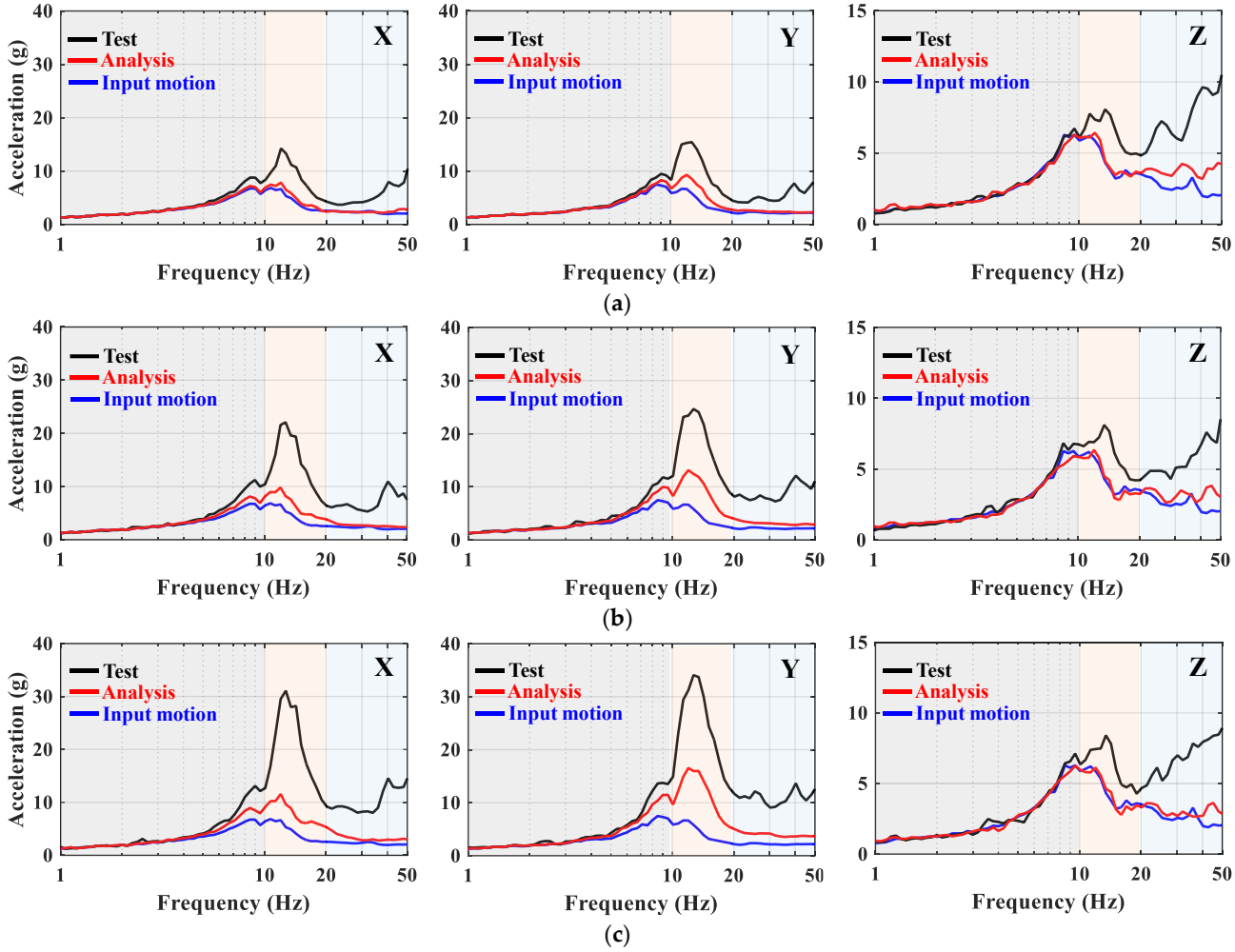


Figure 22. Comparison of FRS (EQ3): (**a**) A2; (**b**) A3; (**c**) A4.

Table 9. Calculation results for average over the frequency range and R_{Avg}.

Type		Direction	EQ1			EQ2			EQ3		
			1–10 Hz	10–20 Hz	20–50 Hz	1–10 Hz	10–20 Hz	20–50 Hz	1–10 Hz	10–20 Hz	20–50 Hz
A1		X	1.020	1.561	0.704	2.047	3.145	1.443	3.040	4.568	2.269
		Y	1.040	1.557	0.658	2.113	3.014	1.390	3.129	4.474	2.177
		Z	0.722	1.259	0.640	1.501	2.758	1.589	2.305	4.571	2.635
Average (g)	Test	X	1.114	2.409	0.955	2.253	5.351	2.215	3.425	9.141	5.196
	A2	Y	1.139	2.575	0.943	2.309	5.582	2.117	3.465	10.580	5.240
		Z	0.727	1.637	0.785	1.503	3.291	1.707	2.318	6.509	7.264
		X	1.191	3.424	1.224	2.390	8.275	3.048	3.759	14.642	7.078
	A3	Y	1.234	3.620	1.267	2.504	8.459	3.248	3.890	17.640	8.846
		Z	0.722	1.606	0.772	1.486	3.274	1.886	2.367	6.269	5.521
		X	1.262	4.422	1.504	2.580	11.012	4.061	4.072	20.477	10.061
	A4	Y	1.302	4.584	1.564	2.647	11.156	4.246	4.303	23.979	10.976
		Z	0.716	1.617	0.794	1.503	3.441	1.907	2.355	6.369	6.726
	Analysis	X	1.036	1.775	0.842	2.082	3.549	1.734	3.113	5.272	2.402
	A2	Y	1.083	2.143	0.794	2.175	4.113	1.570	3.246	6.149	2.432
		Z	0.728	1.419	1.115	1.599	3.087	2.240	2.312	4.731	3.764
		X	1.109	2.261	0.940	2.211	4.400	1.797	3.314	6.706	2.756
	A3	Y	1.178	3.009	1.020	2.378	5.854	1.983	3.539	9.036	3.166
		Z	0.720	1.289	0.857	1.518	2.872	1.703	2.258	4.512	3.248
		X	1.176	2.683	1.058	2.361	5.233	2.169	3.485	8.105	3.362
	A4	Y	1.257	3.770	1.259	2.534	7.540	2.409	3.791	11.668	4.007
		Z	0.727	1.340	0.810	1.493	2.906	1.701	2.279	4.513	3.075

Table 9. *Cont.*

Type		Direction		EQ1			EQ2			EQ3		
				1–10 Hz	10–20 Hz	20–50 Hz	1–10 Hz	10–20 Hz	20–50 Hz	1–10 Hz	10–20 Hz	20–50 Hz
R_{Avg} (g/g)	Test	A2	X	1.092	1.543	1.356	1.101	1.701	1.534	1.126	2.001	2.290
			Y	1.095	1.654	1.432	1.093	1.852	1.523	1.107	2.365	2.407
			Z	1.007	1.300	1.225	1.002	1.193	1.074	1.006	1.424	2.757
		A3	X	1.169	2.194	1.737	1.168	2.631	2.112	1.236	3.205	3.119
			Y	1.186	2.325	1.925	1.185	2.807	2.337	1.243	3.943	4.063
			Z	1.001	1.275	1.206	0.990	1.187	1.187	1.027	1.371	2.095
		A4	X	1.238	2.833	2.135	1.261	3.501	2.813	1.340	4.482	4.433
			Y	1.252	2.944	2.376	1.253	3.701	3.055	1.375	5.359	5.041
			Z	0.992	1.284	1.241	1.001	1.248	1.200	1.022	1.393	2.553
	Analysis	A2	X	1.016	1.137	1.196	1.017	1.128	1.201	1.024	1.154	1.059
			Y	1.041	1.376	1.206	1.029	1.365	1.129	1.037	1.374	1.117
			Z	1.008	1.127	1.742	1.066	1.119	1.410	1.003	1.035	1.428
		A3	X	1.088	1.449	1.335	1.080	1.399	1.245	1.090	1.468	1.214
			Y	1.133	1.933	1.549	1.125	1.942	1.427	1.131	2.020	1.454
			Z	0.998	1.023	1.338	1.011	1.042	1.072	0.979	0.987	1.233
		A4	X	1.154	1.719	1.502	1.153	1.664	1.503	1.146	1.774	1.481
			Y	1.209	2.421	1.912	1.199	2.502	1.734	1.212	2.608	1.841
			Z	1.007	1.064	1.265	0.995	1.054	1.070	0.988	0.987	1.167
PD (%)		A2	X	7.24	30.28	12.55	7.87	40.49	24.35	9.53	53.68	73.53
			Y	5.10	18.30	17.14	5.99	30.30	29.70	6.53	52.97	73.20
			Z	0.17	14.26	34.81	6.22	6.40	27.03	0.27	31.62	63.48
		A3	X	7.16	40.90	26.19	7.76	61.13	51.63	12.59	74.35	87.91
			Y	4.62	18.42	21.65	5.17	36.39	48.33	9.47	64.51	94.59
			Z	0.27	21.91	10.40	2.12	13.07	10.16	4.71	32.60	51.84
		A4	X	7.02	48.95	34.79	8.87	71.14	60.74	15.55	86.57	99.82
			Y	3.48	19.48	21.65	4.34	38.69	55.19	12.64	69.07	93.01
			Z	1.41	18.77	1.95	0.69	16.86	11.43	3.29	34.11	74.50

Table 10. Calculation results for peak over the frequency range and R_{Peak}.

Type		Direction		EQ1			EQ2			EQ3		
				1–10 Hz	10–20 Hz	20–50 Hz	1–10 Hz	10–20 Hz	20–50 Hz	1–10 Hz	10–20 Hz	20–50 Hz
A1			X	1.020	1.561	0.704	2.047	3.145	1.443	3.040	4.568	2.269
			Y	1.040	1.557	0.658	2.113	3.014	1.390	3.129	4.474	2.177
			Z	0.722	1.259	0.640	1.501	2.758	1.589	2.305	4.571	2.635
Peak (g)	Test	A2	X	1.114	2.409	0.955	2.253	5.351	2.215	3.425	9.141	5.196
			Y	1.139	2.575	0.943	2.309	5.582	2.117	3.465	10.580	5.240
			Z	0.727	1.637	0.785	1.503	3.291	1.707	2.318	6.509	7.264
		A3	X	1.191	3.424	1.224	2.390	8.275	3.048	3.759	14.642	7.078
			Y	1.234	3.620	1.267	2.504	8.459	3.248	3.890	17.640	8.846
			Z	0.722	1.606	0.772	1.486	3.274	1.886	2.367	6.269	5.521
		A4	X	1.262	4.422	1.504	2.580	11.012	4.061	4.072	20.477	10.061
			Y	1.302	4.584	1.564	2.647	11.156	4.246	4.303	23.979	10.976
			Z	0.716	1.617	0.794	1.503	3.441	1.907	2.355	6.369	6.726
	Analysis	A2	X	1.036	1.775	0.842	2.082	3.549	1.734	3.113	5.272	2.402
			Y	1.083	2.143	0.794	2.175	4.113	1.570	3.246	6.149	2.432
			Z	0.728	1.419	1.115	1.599	3.087	2.240	2.312	4.731	3.764
		A3	X	1.109	2.261	0.940	2.211	4.400	1.797	3.314	6.706	2.756
			Y	1.178	3.009	1.020	2.378	5.854	1.983	3.539	9.036	3.166
			Z	0.720	1.289	0.857	1.518	2.872	1.703	2.258	4.512	3.248
		A4	X	1.176	2.683	1.058	2.361	5.233	2.169	3.485	8.105	3.362
			Y	1.257	3.770	1.259	2.534	7.540	2.409	3.791	11.668	4.007
			Z	0.727	1.340	0.810	1.493	2.906	1.701	2.279	4.513	3.075

Table 10. *Cont.*

Type		Direction		EQ1			EQ2			EQ3		
				1–10 Hz	10–20 Hz	20–50 Hz	1–10 Hz	10–20 Hz	20–50 Hz	1–10 Hz	10–20 Hz	20–50 Hz
R_{Avg} (g/g)	Test	A2	X	1.092	1.543	1.356	1.101	1.701	1.534	1.126	2.001	2.290
			Y	1.095	1.654	1.432	1.093	1.852	1.523	1.107	2.365	2.407
			Z	1.007	1.300	1.225	1.002	1.193	1.074	1.006	1.424	2.757
		A3	X	1.169	2.194	1.737	1.168	2.631	2.112	1.236	3.205	3.119
			Y	1.186	2.325	1.925	1.185	2.807	2.337	1.243	3.943	4.063
			Z	1.001	1.275	1.206	0.990	1.187	1.187	1.027	1.371	2.095
		A4	X	1.238	2.833	2.135	1.261	3.501	2.813	1.340	4.482	4.433
			Y	1.252	2.944	2.376	1.253	3.701	3.055	1.375	5.359	5.041
			Z	0.992	1.284	1.241	1.001	1.248	1.200	1.022	1.393	2.553
	Analysis	A2	X	1.016	1.137	1.196	1.017	1.128	1.201	1.024	1.154	1.059
			Y	1.041	1.376	1.206	1.029	1.365	1.129	1.037	1.374	1.117
			Z	1.008	1.127	1.742	1.066	1.119	1.410	1.003	1.035	1.428
		A3	X	1.088	1.449	1.335	1.080	1.399	1.245	1.090	1.468	1.214
			Y	1.133	1.933	1.549	1.125	1.942	1.427	1.131	2.020	1.454
			Z	0.998	1.023	1.338	1.011	1.042	1.072	0.979	0.987	1.233
		A4	X	1.154	1.719	1.502	1.153	1.664	1.503	1.146	1.774	1.481
			Y	1.209	2.421	1.912	1.199	2.502	1.734	1.212	2.608	1.841
			Z	1.007	1.064	1.265	0.995	1.054	1.070	0.988	0.987	1.167
PD (%)		A2	X	7.24	30.28	12.55	7.87	40.49	24.35	9.53	53.68	73.53
			Y	5.10	18.30	17.14	5.99	30.30	29.70	6.53	52.97	73.20
			Z	0.17	14.26	34.81	6.22	6.40	27.03	0.27	31.62	63.48
		A3	X	7.16	40.90	26.19	7.76	61.13	51.63	12.59	74.35	87.91
			Y	4.62	18.42	21.65	5.17	36.39	48.33	9.47	64.51	94.59
			Z	0.27	21.91	10.40	2.12	13.07	10.16	4.71	32.60	51.84
		A4	X	7.02	48.95	34.79	8.87	71.14	60.74	15.55	86.57	99.82
			Y	3.48	19.48	21.65	4.34	38.69	55.19	12.64	69.07	93.01
			Z	1.41	18.77	1.95	0.69	16.86	11.43	3.29	34.11	74.50

Table 11. Calculation results for ZPA and R_{ZPA}.

Type		Location	ZPA (45.25 Hz)								
			EQ1			EQ2			EQ3		
			X	Y	Z	X	Y	Z	X	Y	Z
A1			0.653	0.624	0.588	1.392	1.289	1.221	2.055	2.175	2.095
ZPA (g)	Test	A2	0.870	0.804	0.627	2.076	1.832	1.384	7.173	5.868	9.080
		A3	1.085	1.102	0.634	2.813	2.593	1.471	8.091	10.422	7.111
		A4	1.298	1.330	0.606	3.561	3.583	1.480	12.749	10.415	8.387
	Analysis	A2	0.860	0.789	1.132	1.459	1.463	1.634	2.829	2.239	3.867
		A3	0.866	0.919	0.831	1.567	1.726	1.567	2.373	3.023	3.836
		A4	0.963	1.175	0.743	1.980	2.036	1.658	2.982	3.729	3.625
R_{ZPA} (g/g)	Test	A2	1.332	1.288	1.067	1.491	1.421	1.134	3.491	2.697	4.333
		A3	1.661	1.766	1.079	2.021	2.011	1.205	3.938	4.791	3.394
		A4	1.987	2.130	1.030	2.557	2.779	1.213	6.205	4.787	4.002
	Analysis	A2	1.317	1.263	1.925	1.048	1.135	1.338	1.377	1.029	1.845
		A3	1.327	1.473	1.413	1.125	1.339	1.283	1.155	1.390	1.830
		A4	1.474	1.882	1.264	1.422	1.579	1.358	1.451	1.714	1.730
PD (%)		A2	1.16	1.95	57.32	34.91	22.38	16.56	86.87	89.53	80.54
		A3	22.37	18.09	26.84	56.91	40.13	6.29	109.28	110.07	59.85
		A4	29.62	12.35	20.41	57.04	55.04	11.32	124.18	94.55	79.28

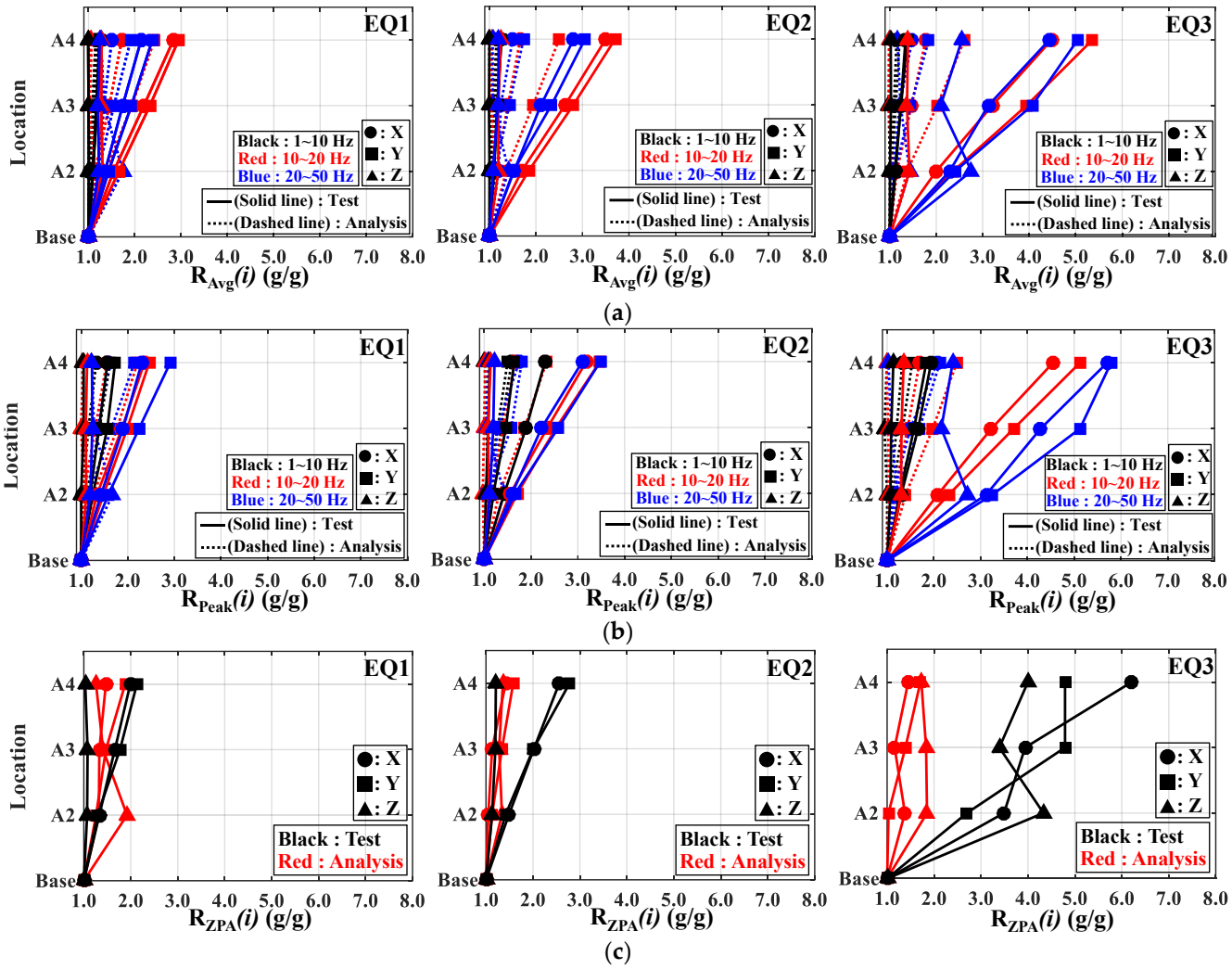


Figure 23. Comparison of FRS amplification ratio: (**a**) average over the frequency range; (**b**) peak over the frequency range; (**c**) ZPA.

Furthermore, Figure 24 presents the differences in the amplification ratio of the FRS at the top of the electrical cabinet model (A4), as derived from the experimental and numerical results. This figure clearly represents the differences and key trends in seismic behavior characteristics previously identified in Figures 22 and 23. In the horizontal directions (X and Y), the discrepancies between experimental and numerical results across all three amplification ratio estimation methods and over the entire frequency range increased relatively linearly with rising seismic motion. However, in EQ3, a pronounced increase in discrepancy was observed in the vertical (Z) direction, particularly in the high-frequency range. Consistent with the results displayed in Figure 22, the analysis of the FRS amplification ratios confirmed that local modes and impact effects within the electrical cabinet can amplify the ICRS, significantly amplifying the vertical component and at high frequencies [29]. It was also confirmed that the seismic responses obtained from the experimental and numerical results tend to be closely aligned when the seismic motion is low. However, as the seismic motion increases, numerical models that simulate boundary conditions using conventional methods may exhibit discrepancies due to different factors, such as anchorage damage and impacts. These discrepancies can result in significant deviations from actual seismic behavior.

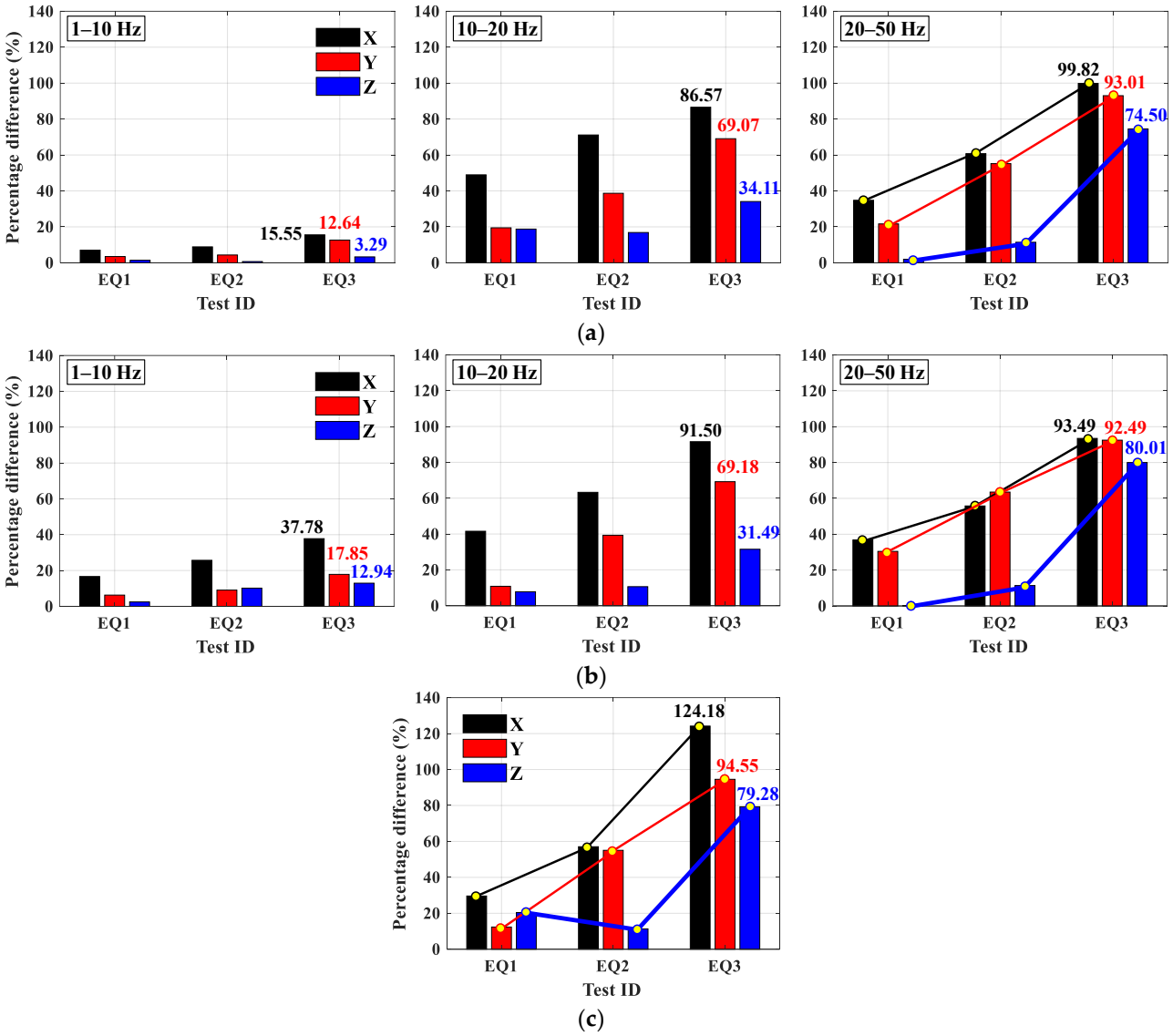


Figure 24. Percentage difference of FRS amplification ratio in A4: (**a**) average over the frequency range; (**b**) peak over the frequency range; (**c**) ZPA.

5. Conclusions

This study aimed to directly compare the seismic behavior characteristics of electrical cabinets installed in NPPs through experimental and numerical methods to identify potential discrepancies. An electrical cabinet model was designed based on the dynamic characteristics of electrical equipment used in Korean-type NPPs, as informed by field surveys. A specimen was fabricated for shaking table tests. The shaking table testing included a resonant frequency search test and a limit state seismic simulation test, conducted under simultaneous tri-axial excitation. The input seismic motion was incrementally increased until structural damage to the specimen occurred. A numerical model was constructed, employing a fixed support to simulate the anchorage boundary conditions, a common practice in numerical analysis. The numerical model's validity was verified using the resonant frequency search test results. Seismic response analysis was performed using the same input seismic motion as the limit state seismic simulation test. The amplification of acceleration response from both the experimental and numerical results were then analyzed to identify and compare differences in seismic behavior characteristics.

The failure of the electrical cabinet model observed during the shaking table test was attributed to the fracture of the anchor bolts. As the input seismic motion increased, impact responses on the cabinet were observed, primarily due to the influence of local modes and the nonlinear behavior of the anchorage. These effects amplified the acceleration response and heightened the likelihood of anchor bolt failure. In actual practice, measures can be taken to prevent failure, such as increasing the design margin by welding the foundation and anchors or adding post-installed anchors. Therefore, it was concluded that reinforcing the support, such as by increasing the number of anchor bolts and enhancing the flexibility of the cabinet's base frame, is important to mitigate the impact responses acting on the electrical cabinet.

RMS and RMQ values were calculated from the acceleration response time histories to quantitatively assess the seismic behavior characteristics. At EQ1, the acceleration responses from the experimental and numerical results demonstrated generally good agreement. However, at EQ3, where anchor bolt damage was observed, the experimental results revealed a significantly amplified acceleration response. The discrepancies between experimental and numerical results reached up to 49.95% and 58.81% in the horizontal direction for RMS and RMQ, respectively. In the vertical direction, the maximum discrepancy was 87.24%, with RMQ reflecting greater variation than RMS. Similarly, R_{RMQ} was consistently evaluated to be greater than R_{RMS}, confirming its ability to capture the effects of nonlinearity and impulsive characteristics.

The seismic behavior characteristics were analyzed and compared by deriving the FRS from the acceleration response time histories. In the low-frequency range, the FRS obtained from the experimental and numerical results exhibited good agreement. However, as the input seismic motion increased, the FRS from the experimental results exhibited greater linear amplification than that from the numerical results across all three directions in the resonant frequency range. Notably, unlike the horizontal directions, where acceleration responses were uniformly amplified within the resonant frequency range, the vertical direction at EQ3 yielded a sharp amplification in the high-frequency range. Moreover, the amplification trend in this range increased with frequency. To quantify the FRS amplification, average and peak values, along with the ZPA, were defined for three frequency ranges: 1–10 Hz, 10–20 Hz, and 20–50 Hz. The amplification ratios (R_{Avg}, R_{Peak}, R_{ZPA}), defined using these three approaches, were calculated accordingly. The results indicate that with increasing input seismic motion, both R_{Avg} and R_{Peak} generally showed a linear increase with respect to the height of the electrical cabinet model, whereas R_{ZPA} exhibited nonlinear variation with height at EQ3. Among the three methods, R_{ZPA} was consistently the largest, while R_{Avg} and R_{Peak} presented generally similar results with respect to height. In the horizontal directions, R_{Avg} in the resonant frequency range (10–20 Hz) was greater at EQ1 and EQ2. In contrast, R_{Peak} was greater than R_{Avg} in the high-frequency range (20–50 Hz). These observations suggest that under relatively low seismic motion, where no anchorage damage occurs, the acceleration response in the resonant frequency range tends to be linearly and uniformly amplified. However, as the seismic motion increases, the resulting anchorage damage, including rocking and impact, contributes significantly to the amplification observed in the high-frequency range.

The comparison of the acceleration response amplification between the experimental and numerical results confirmed that the numerical model, assuming fully fixed boundary conditions with constraints on all degrees of freedom, does not adequately reflect the actual seismic behavior. This limitation may result in the nonlinear characteristics of the anchorage being neglected, potentially leading to an overestimation of seismic performance. Significant differences in behavior were identified due to the superposition of global modes and local modes induced by impact. Unlike the general case where acceleration response

amplification increases linearly with height, the amplification in the electrical cabinet model was found to be nonlinear and could reach its maximum at any location. Furthermore, this nonlinear amplification was observed to contribute to the increase in the ICRS, particularly in the high-frequency range, potentially causing not only structural problems in the cabinet but also inducing alternative failure modes and functional issues in internal equipment. If only relatively low seismic motions are considered in the numerical approach, actual seismic behaviors, such as rocking and impact caused by local anchorage response, may be overlooked. Since such impulsive characteristics have a greater influence on high-frequency responses, especially in the vertical direction, vertical response behavior must also be addressed in numerical studies and seismic evaluations. Consequently, when the numerical model is unable to adequately account for the superposition of global and local modes of the electrical cabinet, or the interaction effects with the concrete foundation caused by the nonlinear behavior of the anchorage—or when damage from large seismic loads must be evaluated—evaluating the cabinet's behavior through experimental methods is appropriate. The findings from this study on the seismic behavior characteristics of the electrical cabinet model are expected to serve as foundational data for evaluating the seismic performance, anchorage configurations, and installation conditions of electrical equipment installed in NPPs.

Author Contributions: Conceptualization, D.-W.Y., B.-G.J. and S.-W.K.; Field survey, D.-W.Y., B.-G.J., S.-W.K., D.H. and H.-P.L.; Experimental test, D.-W.Y., B.-G.J. and S.-W.K.; Methodology, D.-W.Y. and B.-G.J.; Numerical analysis, D.-W.Y. and B.-G.J.; Validation, D.-W.Y. and B.-G.J.; Visualization, D.-W.Y.; Investigation, D.-W.Y. and B.-G.J.; Writing—original draft preparation, D.-W.Y.; Writing—review and editing, D.-W.Y., B.-G.J. and S.-W.K.; Project administration, B.-G.J.; Funding acquisition, H.-P.L. All authors have read and agreed to the published version of the manuscript.

Funding: This work was supported by the Korea Institute of Energy Technology Evaluation and Planning (KETEP) and the Ministry of Trade, Industry and Energy (MOTIE) of the Republic of Korea (No. 20217910100150).

Institutional Review Board Statement: Not applicable.

Informed Consent Statement: Not applicable.

Data Availability Statement: The original contributions presented in this study are included in the article. Further inquiries can be directed to the corresponding author(s).

Conflicts of Interest: Author Hong-Pyo Lee was employed by the company Central Research Institute, Korea Hydro & Nuclear Power Co., Ltd. The remaining authors declare that the research was conducted in the absence of any commercial or financial relationships that could be construed as a potential conflict of interest.

Abbreviations

The following abbreviations are used in this manuscript:

NPP	Nuclear power plant
ICRS	In-cabinet response spectrum
MCC	Motor control center
RRS	Required response spectrum
TRS	Test response spectrum
FRS	Floor response spectrum
ZPA	Zero period acceleration
PD	Percentage difference
RMS	Root mean square
RMQ	Root mean quad

References

1. Goodno, B.J.; Gould, N.C.; Caldwell, P.; Gould, P.L. Effects of the January 2010 Haitian earthquake on selected electrical equipment. *Earthq. Spectra* **2011**, *27*, S251–S276. [CrossRef]
2. Shang, Q.; Zuo, H.; Wen, L.; Li, Z.; Sun, G.; Pan, P.; Wang, T. Seismic resilience of internet data center building with different disaster mitigation techniques. *Resilient Cities Struct.* **2022**, *1*, 42–56. [CrossRef]
3. Ikbal, M.K.H.; Nguyen, D.V.; Kim, S.; Kim, D. Seismic evaluation of different types of electrical cabinets in nuclear power plants considering coupling effects: Experimental and numerical study. *Nucl. Eng. Technol.* **2023**, *55*, 3472–3484. [CrossRef]
4. United States Nuclear Regulatory Commission (USNRC). *Identification of New Unresolved Safety Issues Relating to Nuclear Power Plant Stations (NUREG-0705)*; USNRC: Washington, DC, USA, 1981.
5. United States Nuclear Regulatory Commission (USNRC). *Seismic Qualification of Equipment in Operating Nuclear Power Plants (NUREG-1030)*; USNRC: Washington, DC, USA, 1987.
6. International Atomic Energy Agency (IAEA). *Seismic Design and Qualification for Nuclear Power Plants*; IAEA: Vienna, Austria, 2004.
7. Lin, F.R.; Chai, J.F.; Lai, Z.Y.; Chou, P.F.; Wu, Y.C. Experimental study for seismic demands on in-cabinet equipment in NPPs. *J. Chin. Inst. Eng.* **2014**, *37*, 833–844. [CrossRef]
8. Chang, S.J.; Jeong, Y.S.; Eem, S.H.; Choi, I.K.; Park, D.U. Evaluation of MCC seismic response according to the frequency contents through the shake table test. *Nucl. Eng. Technol.* **2021**, *53*, 1345–1356. [CrossRef]
9. Jeong, Y.S.; Eem, S.H.; Jeon, B.G.; Park, D.U. Evaluation of structural and functional behavior of battery charger for low/high-frequency motions in NPP. *Appl. Sci.* **2022**, *12*, 4328. [CrossRef]
10. Jeon, B.G.; Kim, S.W.; Chang, S.J.; Park, D.U.; Lee, H.P. Seismic behavior of simplified electrical cabinet model considering cast-in-place anchor in uncracked and cracked concretes. *Nucl. Eng. Technol.* **2023**, *55*, 4252–4265. [CrossRef]
11. Nagai, M.; Minakawa, Y.; Hibino, K.; Takamatsu, N.; Ishida, N.; Yoshimura, E.; Maruyama, N.; Furuya, O. Shaking Table Test of Electrical Cabinet Considering Shock Vibration. In Proceedings of the 27th International Conference on Structural Mechanics in Reactor Technology, Yokohama, Japan, 3–8 March 2024.
12. Zuo, H.; Sun, G.; Zhang, P.; Wang, M.; Li, J.; Shang, Q.; Wang, T. Shaking table tests of a switching power cabinet considering physical damage and functionality loss. *Soil Dyn. Earthq. Eng.* **2024**, *177*, 108421. [CrossRef]
13. Shang, Q.; Zuo, H.; Zhang, X.; Li, Z.; Sun, G.; Zhang, P.; Li, J.; Wang, T. Shaking table tests of power distribution cabinets: Physical damage, post-earthquake functionality and seismic response evaluation. *Structures* **2024**, *62*, 106208. [CrossRef]
14. Salman, K.; Tran, T.T.; Kim, D. Seismic capacity evaluation of NPP electrical cabinet facility considering grouping effects. *J. Nucl. Sci. Technol.* **2020**, *57*, 800–812. [CrossRef]
15. Tran, T.T.; Cao, A.T.; Kim, D.; Chang, S.K. Seismic vulnerability of cabinet facility with tuned mass dampers subjected to high-and low-frequency earthquakes. *Appl. Sci.* **2020**, *10*, 4850. [CrossRef]
16. Lee, S.M.; Jeon, B.G.; Kim, S.W.; Yun, D.W.; Jung, W.Y. Evaluating the applicability of seismic retrofit of an electric cabinet in a power plant. *Struct. Build.* **2024**, *177*, 589–605. [CrossRef]
17. Gupta, A.; Rustogi, S.K.; Gupta, A.K. Reconciliation of Experimental and Analysis Results for Switchgear Incabinet Spectra. In Proceedings of the 15th International Conference on Structural Mechanics in Reactor Technology, Seoul, Republic of Korea, 15–20 August 1999.
18. Ries, M.; Hahn, T.; Henkel, F.O. Seismic Qualification of an Electrical Cabinet: Comparison of Analysis and Test Results. In Proceedings of the 24th International Conference on Structural Mechanics in Reactor Technology, Busan, Republic of Korea, 20–25 August 2017.
19. Son, H.; Park, S.; Jeon, B.G.; Jung, W.Y.; Choi, J.; Ju, B.S. Seismic qualification of electrical cabinet using high-fidelity simulation under high frequency earthquakes. *Sustainability* **2020**, *12*, 8048. [CrossRef]
20. Son, H.; So, W.B.; Jeon, B.G.; Jung, W.Y.; Ju, B.S. Dynamic characteristics of double-door electrical cabinet by 3D finite element analysis model. *J. Korean Soc. Adv. Compos. Struct.* **2020**, *11*, 60–66. [CrossRef]
21. Salman, K.; Cho, S.G. Effect of frequency content of earthquake on the seismic response of interconnected electrical equipment. *CivilEng* **2020**, *1*, 198–215. [CrossRef]
22. Jeon, B.G.; Son, H.Y.; Eem, S.H.; Choi, I.K.; Ju, B.S. Dynamic characteristics of single door electrical cabinet under rocking: Source reconciliation of experimental and numerical findings. *Nucl. Eng. Technol.* **2021**, *53*, 2387–2395. [CrossRef]
23. Ruggieri, S.; Vukobratović, N. The influence of torsion on acceleration demands in low-rise RC buildings. *Bull. Earthq. Eng.* **2024**, *22*, 2433–2468. [CrossRef]
24. Llambias, J.M.; Sevant, C.J.; Shepherd, D.J. Non-Linear Response of Electrical Cubicles for Fragility Estimation. In Proceedings of the 10th International Conference on Structural Mechanics in Reactor Technology, Anaheim, CA, USA, 22–27 August 1989.
25. Yang, J.; Rustogi, S.K.; Gupta, A. Rocking stiffness of mounting arrangements in electrical cabinets and control panels. *Nucl. Eng. Des.* **2003**, *219*, 127–141. [CrossRef]
26. Yun, D.W.; Jeon, B.G.; Jung, W.Y.; Chang, S.J.; Shin, Y.J. Analysis of anchorage behavior characteristics of the electrical cabinet using shaking table tests. *Korean Soc. Noise Vib. Eng.* **2019**, *29*, 43–50. [CrossRef]

27. Cho, S.G.; Salman, K. Seismic demand estimation of electrical cabinet in nuclear power plant considering equipment-anchor-interaction. *Nucl. Eng. Technol.* **2022**, *54*, 1382–1393. [CrossRef]
28. Federal Emergency Management Agency (FEMA). *Reducing the Risks of Nonstructural Earthquake Damage—A Practical Guide (FEMA E-74)*; FEMA: Washington, DC, USA, 2012.
29. Merz, K.L.; Ibanez, P. Guidelines for estimation of cabinet dynamic amplification. *Nucl. Eng. Des.* **1990**, *123*, 247–255. [CrossRef]
30. Electric Power Research Institute (EPRI). *The Effects of High-Frequency Ground Motion on Structures, Components, and Equipment in Nuclear Power Plants*; EPRI: Palo Alto, CA, USA, 2007.
31. Bandyopadhyay, K.K.; Hofmayer, C.H.; Kassir, M.K.; Pepper, S.E. *Dynamic Amplification of Electrical Cabinets (NUREG/CR-5203)*; Brookhaven National Laboratory (BNL): New York, NY, USA, 1988.
32. Lee, B.J.; Berak, E.G.; Passalugo, P.N. Effect of base shim plates on seismic qualification of electrical control panels. *Am. Soc. Mech. Eng.* **1990**, *197*, 301–306.
33. Lee, B.J.; Abou-Jaoude, C.; De Estrada, M. Issues of control panel rigidity in seismic qualification. *Seism. Eng.* **1991**, *220*, 283–287.
34. Lee, B.J.; Abou-Jaoude, C. Effect of base uplift on dynamic response of electrical and mechanical equipment. *Seism. Eng.* **1992**, *237*, 45–150.
35. Latif, A.; Salman, K.; Kim, D. Seismic response of electrical cabinets considering primary-secondary structure interaction with contact nonlinearity of anchors. *J. Nucl. Sci. Technol.* **2022**, *59*, 757–767. [CrossRef]
36. Song, J.; Pan, Y.; Wang, T.; Chen, Q. Seismic response and fragility analysis of railway station typical signal cabinets. *Structures* **2024**, *68*, 107185. [CrossRef]
37. Lin, W.T.; Wu, Y.C.; Huang, C.C. Frequency analysis of the motor control centers in a nuclear power plant using testing and simulating methods. *Appl. Mech. Mater.* **2014**, *479–480*, 1045–1050. [CrossRef]
38. American Concrete Institute (ACI). *Qualification of Post-Installed Mechanical Anchors in Concrete and Commentary (ACI 355.2-07)*; ACI: Farmington Hills, MI, USA, 2007.
39. *ASTM A36/A36M-19*; Standard Specification for Carbon Structural Steel. American Society for Testing and Materials (ASTM) International: Conshohocken, PA, USA, 2019.
40. Gupta, A.; Rustogi, S.K.; Gupta, A.K. Ritz vector approach for evaluating incabinet response spectra. *Nucl. Eng. Des.* **1999**, *190*, 255–272. [CrossRef]
41. Salman, K.; Tran, T.T.; Kim, D. Grouping effect on the seismic response of cabinet facility considering primary-secondary structure interaction. *Nucl. Eng. Technol.* **2020**, *52*, 1318–1326. [CrossRef]
42. Singh, S.; Gupta, A. Understanding the seismic response of electrical equipment subjected to high–frequency ground motions. *Prog. Nucl. Energy* **2021**, *140*, 103915. [CrossRef]
43. Chang, S.J.; Lee, Y.L.; Jeong, Y.S.; Kim, J.B.; Park, D.U. *Seismic Test Report for 1st Limit State Test of Load Center*; Seismic Research and Test Center (SESTEC), Institute for Research and Business Development Foundation, Pusan National University: Yangsan, Republic of Korea, 2024.
44. Jeon, B.G.; Park, D.U.; Kim, S.W.; Chang, S.J.; Eem, S.; Park, J. A case study on the failure of the electrical panel of nuclear power plants by shaking table tests. *Nucl. Eng. Technol.* **2025**, *57*, 103533. [CrossRef]
45. *KS D 3568*; Carbon Steel Square Pipes for General Structural Purposes. Korea Agency for Technology and Standards (KS): Eumseong, Republic of Korea, 2023.
46. Rivera-Rosarino, H.T.; Powell, J.S. *Installation Torque Tables for Noncritical Applications (NASA/TM-2017-219475)*; National Aeronautics and Space Administration (NASA): Washington, DC, USA, 2017.
47. *IEEE Std 344*; IEEE Standard for Seismic Qualification of Equipment for Nuclear Power Generating Stations. The Institute of Electrical and Electronics Engineers (IEEE): Piscataway, NJ, USA, 2013.
48. Kim, J.B.; Kim, S.K.; Seo, K.S.; Lee, J.C. Stress-Strain Curves of Mild Carbon Steels for Decommissioning Wastes Transportation Container. In Proceedings of the Korean Nuclear Society Autumn Meeting, Seoul, Republic of Korea, 23–25 October 2019.
49. Kang, H.S.; Kim, T.S. An experimental study on buckling behaviors of cold-formed carbon steel square hollow section compressive members under a concentric axial load. *J. Archit. Inst. Korea* **2022**, *38*, 273–282.
50. United States Nuclear Regulatory Commission (USNRC). *Recommendations for Revision of Seismic Damping Values in Regulatory Guide 1.61 (NUREG/CR-6919)*; USNRC: Washington, DC, USA, 2006.
51. Jeon, B.G.; Chang, S.J.; Kim, S.W.; Park, D.U.; Chun, N. Experimental study on the acceleration amplification ratio of cable terminations for electric power facilities. *Energies* **2024**, *17*, 5641. [CrossRef]
52. Olieman, M.; Marin-Perianu, R.; Marin-Perianu, M. Measurement of dynamic comfort in cycling using wireless acceleration sensors. *Procedia Eng.* **2012**, *34*, 568–573. [CrossRef]
53. Shah, S. Mesh Discretization Error and Criteria for Accuracy of Finite Element Solutions. In Proceedings of the 4th ASEAN ANSYS Users Conference, Singapore, 5–6 November 2002.
54. Nahar, T.T.; Cao, A.T.; Kim, D. Effective safety assessment of aged concrete gravity dam based on the reliability index in a seismically induced site. *Appl. Sci.* **2021**, *11*, 1987. [CrossRef]

55. Turja, S.D.; Islam, M.R.; Van Nguyen, D.; Kim, D. An efficient numerical modeling approach for coupled electrical cabinets in nuclear power plants. *Nucl. Eng. Technol.* **2024**, *56*, 3512–3527. [CrossRef]
56. *IEEE Std 693*; IEEE Recommended Practice for Seismic Design of Substations. The Institute of Electrical and Electronics Engineers (IEEE): Piscataway, NJ, USA, 2018.
57. Park, S.J.; Chun, N.; Hwang, K.M.; Moon, J.; Song, J.K. Evaluation of Acceleration Amplification Factors Based on the Structural Type of Substation for the Seismic Design of Power Facilities. *J. Comput. Struct. Eng. Inst. Korea* **2020**, *33*, 159–169. [CrossRef]

Disclaimer/Publisher's Note: The statements, opinions and data contained in all publications are solely those of the individual author(s) and contributor(s) and not of MDPI and/or the editor(s). MDPI and/or the editor(s) disclaim responsibility for any injury to people or property resulting from any ideas, methods, instructions or products referred to in the content.